ATG16L1 induces the formation of phagophore-like membrane cups

Jagan Mohan, Satish B Moparthi, Christine Girard-Blanc, Daniele Campisi, Stéphane Blanchard, Charlotte Nugues, Sowmya Rama, Audrey Salles, Esthel Pénard, Stéphane Vassilopoulos, et al.

ATG16L1 induces the formation of phagophore-like membrane cups

Jagan Mohan, Satish B Moparthi, Christine Girard-Blanc, Daniele Campisi, Stéphane Blanchard, Charlotte Nugues, Sowmya Rama, Audrey Salles, Esthel Pénard, Stéphane Vassilopoulos, et al.

ATG16L1 induces the formation of phagophore-like membrane cups

Authors: Jagan Mohan[1]†, Satish B. Moparthi[1]†‡, Christine Girard-Blanc[1], Daniele Campisi[1], Stéphane Blanchard[1], Charlotte Nugues[1], Sowmya Rama[1], Audrey Salles[2], Esthel Pénard[3], Stéphane Vassilopoulos[4], and Thomas Wollert[1]

Affiliations:

[1] Membrane Biochemistry and Transport, Institut Pasteur, Université de Paris, UMR3691 CNRS, 75015, Paris, France

[2] Unit of Technology and Service Photonic BioImaging (UTechS PBI), C2RT, Institut Pasteur, Université de Paris, France.

[3] Ultrastructural BioImaging Core Facility (UBI), C2RT, Institut Pasteur, Université Paris Cité, Paris, France.

[4] Sorbonne Université, Institut National de la Santé et de la Recherche Médicale, Association Institut de Myologie, Centre de Recherche en Myologie, UMRS 974 CNRS, Paris, France

† Both authors contributed equally to this work.

‡ Current address : Sorbonne Université, Institut National de la Santé et de la Recherche Médicale, Association Institut de Myologie, Centre de Recherche en Myologie, UMRS 974 CNRS, Paris, France

Corresponding authors: Stéphane Vassilopoulos, s.vassilopoulos@institut-myologie.org; Thomas Wollert, thomas.wollert@pasteur.fr

Abstract

The hallmark of nonselective autophagy is the formation of cup-shaped phagophores that capture bulk cytoplasm. The process is accompanied by the conjugation of LC3B to phagophores by an E3-ligase complex comprising ATG12–ATG5 and ATG16L1. Here, we combined two complementary reconstitution approaches to reveal the function of LC3B and its ligase complex during phagophore expansion. We found that LC3B forms together with ATG12–ATG5-ATG16L1 a membrane coat that remodels flat membranes into cups that closely resemble phagophores. Mechanistically, we revealed that cup formation strictly depends on a close collaboration of LC3B and ATG16L1. Moreover, only LC3B, but no other member of the ATG8 protein family, promotes cup formation. ATG16L1 truncates which lacked the C-terminal membrane binding domain catalyzed LC3B lipidation but failed to assemble coats, did not promote cup formation and inhibited the biogenesis of nonselective autophagosomes. Our results thus demonstrate that ATG16L1 and LC3B induce and stabilize the characteristic cup-like shape of phagophores.

Main Text

Macroautophagy (autophagy in the following) is a highly conserved pathway that sequesters cytoplasmic material in double-membrane bound autophagosomes and delivers it to lysosomes for degradation[1]. Autophagy maintains cellular homeostasis by degrading unwanted or damaged cytoplasmic components[2] and by recycling bulk cytoplasm during periods of nutrient deprivation or cytotoxic stresses[3]. Selective autophagy is thus tightly coupled to the presence of superfluous or damaged material, while nonselective autophagy occurs independently of specific cargo[4].

The formation of autophagosomes is driven by autophagy related (ATG) proteins that assemble at sites of phagophore formation in a highly coordinated and sequential manner. Initiation of autophagy depends on the activation of the ULK1 complex which is followed by the recruitment of the phosphatidylinositol (PtdIns)-3-kinase complex (PI3K)[5] and of ATG9 vesicles, which nucleate phagophores[6].

The expansion of phagophores depends on the mobilization of various lipid reservoirs, including organelles[7–10], lipid droplets[11] or direct lipid transfer from the ER[12]. Moreover, this process is accompanied by the conjugation of ubiquitin-like ATG8 proteins to the lipid phosphatidylethanolamine (PE)[13]. The reaction is catalyzed by a ubiquitin-like conjugation system comprising the E1 enzyme ATG7, the E2 enzyme ATG3, and an E3 ligase complex that consists of the ATG12–ATG5 conjugate and the coiled-coil protein ATG16L1[14–17]. The latter is recruited to early phagophores by the PtdIns(3)phosphate binding protein WIPI2[18].

The ATG8 family of proteins comprises microtubule-associated protein 1 light chain 3 (LC3)A, LC3B and LC3C as well as gamma-amino-butyric acid receptor-associated protein (GABARAP), GABARAPL1 and GABARAPL2. All ATG8 proteins can tether cargo to phagophore membranes in selective autophagy[4]. LC3C and GABARAPs also recruit autophagosomes to lysosomes[19,20] and GABARAPs promote autophagosome-lysosome fusion[21]. Although LC3 proteins are dispensable for autophagy, they appear to regulate the size of autophagosomes[21–24]. Moreover, nonselective phagophores continuously acquire LC3B and the amount of LC3B correlates with the size of phagophores[25]. How LC3B promotes phagophore expansion in nonselective autophagy remains, however, obscure.

Here, we applied an integrated and multidisciplinary approach to obtain mechanistic insights into the formation of nonselective autophagosomes. In vitro reconstitutions on model

membranes demonstrated that LC3B and ATG12–ATG5-ATG16L1 formed a continuous membrane coat composed of well-defined particles and remodeled flat membranes into cups that closely resembled nonselective phagophores. Targeting of ATG16L1 to the plasma membrane induced the formation of similar LC3B- and ATG16L1-positive membrane cups. Based on our findings, we propose that ATG16L1 assembles with ATG12–ATG5 and LC3B into coats to shape nonselective phagophores and to support their expansion.

Results

Reconstituting lipidation of LC3B on GUVs in vitro

Nonselective autophagy is characterized by a marked increase in the number of LC3B-positive autophagosomes, suggesting that LC3B fulfills important functions in this process. To identify novel functions of LC3B in nonselective autophagy, we reconstituted the enzymatic conjugation of LC3B to model membranes in vitro (**Fig. 1a**). We first purified all components of the conjugation system including the proteolytically activated form of LC3B ($LC3B^{G120}$, **Extended Data Fig. 1a**) and confirmed the catalytic activity of ATG7 and ATG3 (**Extended Data Fig. 1b**). We then conjugated Alexa488 labeled $LC3B^{G120}$ to Giant Unilamellar Vesicles (GUVs) using ATG7, ATG3, ATP, and the E3-ligase ATG12–ATG5-ATG16L1. We followed conjugation of LC3B in real time by confocal microscopy (**Movie S1**). The fluorescence of $LC3B^{G120}$ increased over time and reached a plateau after ~80 min (**Fig. 1b**). Remarkably, the conjugation reaction induced the formation of small membrane buds on GUVs (**Fig. 1b**, **c**), which were initially mobile but lost mobility with increasing $LC3B^{G120}$ levels (**Movies S1 and S2**). Similar deformations were also observed after conjugating LC3B to Supported Lipid Bilayers (SLBs, **Fig. 1d**). Previous studies by others and we reported that enzymatic conjugation of yeast Atg8 to GUVs induces membrane deformations, but the specific contribution of Atg8 remained unknown[26,27]. We thus tested whether enzymatic conjugation of human LC3B to membranes is sufficient to induce deformations by reconstituting the reaction with ATG7, ATG3, and ATG12–ATG5 but excluding ATG16L1. We found that $LC3B^{G120}$ was not conjugated to membranes, suggesting that the activity of ATG12–ATG5 depends on its interaction with ATG16L1. We thus reconstituted the reaction using a minimal E3-ligase complex comprising only the ATG5 interacting region (AIR) of ATG16L1 ($ATG12–ATG5-ATG16L1^{NT}$; NT =

residues 11-43)[28]. We found that LC3B^{G120} was efficiently conjugated to GUVs, but membrane deformations were not observed (**Fig. 1e**), indicating that membrane remodeling depends on full-length ATG16L1 (ATG16L1^{FL}). We next determined the mobility of LC3B and ATG16L1 on model membranes using fluorescence recovery after photobleaching (FRAP). We found that fluorescent labeled LC3B^{G120} and ATG16L1^{FL} did not exchange with the bulk solution, consistent with the conjugation of LC3B to membranes. Furthermore, the lateral diffusion of LC3B and ATG16L1^{FL} was strongly attenuated (**Fig. 1f** and **Extended Data Fig. 1c, d**). In conjugations with ATG12–ATG5-ATG16L1^{NT}, the fluorescence of a substantial fraction of LC3B^{G120} recovered rapidly by lateral diffusion (**Extended Data Fig. 1e**). We concluded that ATG16L1 immobilizes LC3B on membranes by limiting its two-dimensional diffusion.

LC3B and ATG12–ATG5-ATG16L1 form a protein coat on membranes in vitro

To reveal how ATG16L1 immobilizes LC3B, we conjugated LC3B to SLBs using the complete conjugation machinery including ATG12–ATG5-ATG16L1^{FL} and characterized the topology of SLBs by atomic force microscopy (AFM). In the absence of proteins, SLBs were perfectly flat and possessed a height of 5 ± 1 nm (**Fig. 2a**). Conjugating LC3B to these membranes induced the formation of a continuous protein layer, reminiscent of a protein coat. The total height of the protein decorated membrane was found to be 22 ± 2 nm (**Fig. 2b**). Consistent with our GUV experiments, LC3B was entirely immobilized on SLBs (**Extended Data Fig. 2a**). In conjugation reactions with ATG12–ATG5-ATG16L1^{NT}, no such protein coat was formed. Instead, mobile particles with a mean diameter of 70 ± 10 nm and a height of 23 ± 3 were observed (**Fig. 2c**), demonstrating that ATG16L1 is an essential component of this coat.

We next aimed to identify critical domains in ATG16L1 by reconstituting reactions using C-terminal ATG16L1 truncations (**Fig. 2d**). We first removed the WD-domain of ATG16L1 which is known to be dispensable for canonical autophagy[29]. The corresponding ATG12–ATG5-ATG16L1^{307} complex catalyzed LC3B^{G120} lipidation and immobilized LC3B^{G120} (mobile fraction = 9 ± 5 %, **Fig. 2e, f** and **Extended Data Fig. 2b**). Additional truncation of a part of the C-terminal lipid binding domain[30] (ATG16L1^{264}) impaired coat formation as evident by an increase in the mobile LC3B^{G120} fraction to 23 ± 8 % (**Fig. 2e, f** and **Extended Data Fig. 2b**). An even stronger effect was observed

when the entire C-terminal membrane binding domain was removed (ATG16L1^{230}, mobile fraction = 38 ± 13 %), or if only the AIR was left (ATG16L1^{NT}, mobile fraction = 53 ± 10 %, **Fig. 2e, f** and **Extended Data Fig. 2b**). In conclusion, we found that the WD-domain of ATG16L1 is dispensable while coiled-coil and membrane binding domains are required for coat formation. We next reconstituted LC3B lipidation on SLB using ATG12–ATG5-ATG16L1^{307} and characterized the topology of the ATG16L1^{307} induced membrane coat by AFM. We found that the corresponding coat was less dense and possessed a striated appearance (**Extended Data Fig. 2c**). Furthermore, the coat was with a height of 11 ± 2 nm significantly thinner than the coat formed by ATG16L1^{FL} (22 ± 2 nm), demonstrating that the WD domain, which has a size of approximately 8 nm and is connected to the membrane binding domain of ATG16L1 by a long unstructured region, could well account for the increased thickness and the smoother appearance of the coat. Moreover, the 30 nm long coiled coil domain of ATG16L1 can only be accommodated in both types of coats if it is in close contact with the membrane, which is consistent with the presence of multiple membrane binding regions in ATG16L1[30,31]. Apart from ATG16L1, both coats contain LC3B with a size of 4.6 nm and ATG12–ATG5, which is 6 nm in size. The size of the resulting complex is thus similar to the height of the ATG16L1^{307} containing coat.

ATG16L1 remodels flat membranes into phagophore-like cups

So far, we demonstrated that the immobilization of LC3B by ATG16L1 is driven by the formation of a protein coat comprising LC3B and ATG12–ATG5-ATG16L1. Our next aim was to reveal whether conjugation of LC3B to SLBs induced membrane deformations. Since AFM is not suited to characterize such membrane remodeling events in the presence of recombinant proteins, we established a new method that combines in vitro reconstitution and production of metal replicas for Platinum Replica Electron Microscopy (PREM). We found that in conjugation reactions with ATG12–ATG5-ATG16L1^{FL}, the flat SLB was deformed into many cup-like structures with diameters between 150 and 300 nm and a well-defined rim of 25 ± 3 nm (**Fig. 3a** and **Movie S3**). We also observed premature cups (15 ± 2 %) and flat membrane rims (21 ± 3 %), suggesting that these structures represent cup intermediates (**Fig. 3b**). Consistent with our AFM experiments, we observed a thin and smooth coat covering extended areas of flat membranes and cups (**Fig. 3a**).

To reveal the specific contribution of ATG16L1 in the formation of these structures, we performed reconstitutions using ATG16L1^{NT}, which contained only the AIR (aa 11-47). In these reactions, the integrity of SLBs was maintained, no protein coat was formed, and membrane deformations were not observed. Instead, many small aggregates, similar to those observed by AFM, and an otherwise amorphous protein layer without substructure was detected (**Fig. 3c**). This result demonstrates that ATG16L1 is essential for cup formation.

To identify ATG16L1 domains or motifs that are important for membrane remodeling, we next performed reconstitutions with C-terminal truncates of ATG16L1. We first tested ATG16L1^{307}, which lacked the C-terminal WD-domain, but retained the capacity to fully immobilize LC3B on membranes. We identified similar characteristic membrane deformations as in reactions with ATG16L1^{WT}. Moreover, the number of expanded (55 ± 4 %) or premature membrane cups (20 ± 1 %) and rims (25 ± 3 %) was similar as in reconstitutions with ATG16L1^{WT} (**Fig. 3b**, **d** and **Movie S4**). This demonstrates that the WD domain is not required for cup formation, which is consistent with previous studies reporting that the WD domain is dispensable for autophagy[29]. Interestingly, the membrane coat formed by ATG16L1^{307} was not smooth as in reconstitutions with ATG16L1^{WT} but composed of closely packed uniform particles with a diameter of 39 ± 5 nm (**Fig. 3d**). A similar morphological difference of the two coats was observed by AFM, suggesting that the WD domain covers the particle-like substructure of the ATG16L1^{WT} coat.

Next, we performed reconstitutions using ATG16L1^{264}, in which half of the recently characterized C-terminal membrane binding domain was missing[30]. We found that SLBs were covered with a less dense protein coat of more dispersed particles (**Fig. 3e**), which explains the higher mobility of LC3B that we observed in corresponding FRAP experiments (**Fig. 2e, f** and **Extended Data Fig. 2b**). However, the morphology and size of particles in reconstitution with either ATG16L1^{264} or ATG16L1^{307} was identical, arguing that the composition of these particles remained identical. In terms of membrane deformations, we observed a remarkable difference. In reconstitutions with ATG16L1^{264}, the number of expanded membrane cups was strongly reduced (14 ± 2 % compared to 64 ± 3 % for ATG16L1^{FL}), but significantly more premature cups (48 ± 4 %) and rims (38 ± 4 %) were observed (**Fig. 3b**, **e**).

To corroborate the involvement of the C-terminal membrane binding domain in membrane remodeling, we next performed reconstitutions with ATG16L1^{230} which lacked the entire domain. In these reactions, significantly smaller particles with a diameter of 28 ± 5 nm were detected (**Fig. 3f**). According to our FRAP experiments, these particles remain mobile, suggesting that they are not interconnected. More importantly, very few expanded cups (3 ± 2 %) were observed and the number of premature cups was also significantly smaller (37 ± 3 %) compared to reactions with ATG16L1^{264} (p=0.002). Flat, rim-like structures were the most abundant in these reactions (60 ± 3 %, **Fig. 3b**, **f**), demonstrating that the C-terminal membrane binding domain is essential for both, the formation of cups and the assembly of an immobile membrane coat.

Finally, we tested cup formation by an ATG16L1 variant that contained enough of the coiled coil (ATG16L1^{207}) to retain its dimeric state[32]. In corresponding reconstitutions, large areas of SLBs were covered by a homogenously dispersed layer of proteins without obvious substructure. The majority of membrane deformations most closely resemble rim-like structures (71 ± 6 %, **Fig. 3b**, **g**), but these structures were often unclosed, branched and less well-defined (**Fig. 3g**).

In conclusion, our experiments revealed that the C-terminal membrane binding region of ATG16L1 is required for the formation of protein coats composed of densely packed and immobile particles as well as for the remodeling of flat membrane substrates into expanded membrane cups. ATG16L1 variants comprising only the AIR and coiled coil domains do not promote the formation of membrane coats and membrane cups, highlighting the essential function of the C-terminal membrane binding domain.

Reconstituting cup formation in cells

Our in vitro studies demonstrated that ATG16L1 remodels model membranes into phagophore-like cups, suggesting that this process is relevant for phagophore expansion in autophagy. We thus tested whether ATG16L1 also remodels biological membranes in cells. To study the function of ATG16L1 in an unbiased manner independently from canonical autophagy, we uncoupled the Ub-like conjugation machinery from the upstream initiation complexes by targeting WIPI2 to the

plasma membrane (PM). We therefore co-expressed the well-established, plasma membrane-targeted WIPI2-CAAX construct that lacks its PtdIns (3)P binding site[18] with mCherry-ATG16L1 and GFP-LC3B in ATG16L1 knock-out cells. We first confirmed that WIPI2-CAAX recruits ATG16L1 and induces conjugation of LC3B to the PM as reported before (**Fig. 4a**). We next established that targeting of the Ub-like conjugation machinery to the PM occurs independently of the autophagy initiation complexes and does not entail their recruitment. We therefore analyzed the cellular localization of ULK1 and ATG9 and found that both proteins are not recruited to the PM (**Fig. 4b and Extended Data Fig. 3a**). Furthermore, depletion of ULK1 by siRNA (**Fig. 4c** and **Extended Data Fig. 3b**) or treatment with the ULK1 inhibitor SBI-0206965 (**Fig. 4d**) did not interfere with the targeting of LC3B to the PM. By contrast, ATG14, a subunit of the PI3-kinase complex, was recruited to the PM (**Fig. 4b and Extended Data Fig. 3a**), but its depletion by siRNA (**Fig. 4c** and **Extended Data Fig. 3c**) or treatment with the PI3-kinase inhibitor SAR405 (**Fig. 4d**) did not impact on PM-targeting of LC3B. Moreover, PtdIns (3)P was not detected at the PM (**Extended Data Fig. 3d**) and starvation had no significant impact on the recruitment of LC3B (**Fig. 4e**), demonstrating that recruitment of ATG16L1 and conjugation of LC3B to the PM occurs independently of ATG9 and the ULK1- and PI3-kinase complexes.

We next explored the morphology of the PM by PREM of unroofed cells expressing WIPI2-CAAX alone. We did not find any deformations of the PM that resembled those observed in our in vitro reconstitutions. However, we observed enlarged ER-PM contact sites that were covered with ≈20 nm large particles, corresponding most likely to WIPI2 (**Fig. 5a**). Enlarged and particle covered contact sites were also present in cells that co-expressed WIPI2-CAAX and ATG16L1 (**Fig. 5b**). By contrast, much smaller, canonical ER-PM contact site devoid of particles were observed in cells expressing WIPI2 without CAAX-tag (**Extended Data Fig. 4a**) or in transfection control cells (**Extended Data Fig. 4b**).

Given that large areas of the PM were covered with WIPI2-CAAX, we assumed that endogenous protein levels of ATG16L1 and LC3B are not high enough to support the formation of membrane coats and cups, which require high local concentrations. We thus tested whether the formation of membrane cups at the PM can be induced by overexpressing WIPI2-CAAX together with ATG16L1 and LC3B. We indeed observed large membrane cups in cells that expressed all three proteins (**Fig. 5c** and **Movie S5**). Moreover, they closely resembled cups

observed on SLBs in vitro and immunogold labeling of GFP-LC3B and HA-ATG16L1 in PREM samples confirmed the presence of both proteins on such structures (**Fig. 5d**). The particle density of LC3B on cups was 93 ± 11 gold particles / μm^2 with a background staining of 19 ± 4 gold particles / μm^2. For ATG16L1, we found a slightly reduced particle density of 71 ± 14 gold particles / μm^2 with a background density of 11 ± 3 gold particles / μm^2 (**Table S1**).

Interestingly, membrane cups emerged from enlarged ER-PM contact sites (**Fig. 5c**), and never directly at the PM, consistent with the role of these contact sites as platforms for autophagosome formation[33].

Revealing functional contributions of ATG16L1 and LC3B in membrane remodeling

Our in vitro reconstitutions demonstrated the pivotal role of ATG16L1 in remodeling membranes. To reveal whether this holds true in vivo, we first analyzed the distribution of ATG16L1 molecules at the plasma membrane in intact cells that expressed WIPI2-CAAX, LC3B and HA-ATG16L1 using 3D-STORM. We found that ATG16L1 molecules at the PM formed cup-like shapes and protrusion (arrowheads in **Fig. 6a**). In a next step, we correlated protein localization with membrane morphology using a combination of CLEM and PREM. ATG16L1 was found to colocalize to regions with rim-like membrane deformations of positive membrane curvature (diameters between 20 and 100 nm) as well as with flat cup-like profiles. Interestingly, a limited colocalization of LC3B was detected in these regions, suggesting that ATG16L1 is sufficient to induce these membrane remodeling events (**Extended Data Fig. 5a** and **Movie S6**). However, expanded membrane protrusions and cups were only detected in regions in which LC3B and ATG16L1 colocalized, suggesting that LC3B acts in synergy with ATG16L1 (**Fig. 6b**, and **Expanded Data Fig. 5b** and **Movie S7**).

To untangle individual contributions of LC3B and ATG16L1 in cup formation at ER-PM contact sites, we made use of the ATG16L1 variants that we already characterized in vitro. We first expressed $ATG16L1^{207}$ together with WIPI2-CAAX and LC3B in ATG16L1 knockout (KO) cells. Due to the missing WIPI2-binding site, $ATG16L1^{207}$ was not recruited to the PM and LC3B was thus not conjugated. Moreover, the morphology of the PM and the WIPI2-induced compartment was unchanged (**Extended Data Fig. 5c**), confirming that ATG16L1 is required to remodel

membranes. All other tested ATG16L1 variants contained the WIPI2 binding site and were thus recruited together with LC3B to the PM (**Extended Data Fig. 5d**).

In cells expressing ATG16L1^{230}, 66 ± 6 % of membrane protrusions resembled flat rims (**Fig. 6c**, **d** and **Movie S8**), which is consistent with our observation that ATG16L1^{230} induces the formation of flat membrane rims in vitro. Compared to cells expressing ATG16L1^{WT}, much less expanded cups (4 ± 3 %, compared to 42 ± 9 %) and autophagosome-like vesicles (1 ± 1 %, compared to 30 ± 10 %) were observed (**Fig. 6c**). We next investigated whether ATG16L1^{264}, which contains half of the C-terminal membrane binding region, restores cup formation in vivo. We found that ATG16L1^{264} induces indeed more premature (60 ± 9 %) and expanded membrane cups (18 ± 10 %), but autophagosome-like vesicles were scarce (4 ± 5 %, **Fig. 6c**, **e**). By contrast, a strong increase in the number of autophagosome-like vesicles (19 ± 8 %) and expanded cups (49 ± 17 %) was observed in cells expressing ATG16L1^{307} compared to those expressing ATG16L1^{264}. Moreover, fewer shallow cups (24 ± 6 %) and rims (7 ± 3 %) were observed (**Fig. 6c**, **f**). Consistent with our findings in vitro, the overall morphology and number of membrane deformations was similar in cells expressing ATG16L1^{307} or ATG16L1^{WT}. Importantly, even in cells expressing ATG16L1^{WT}, all types of membrane deformations, including autophagosome-like vesicles (30 ± 10 %), expanded cups (42 ± 9 %), premature cups (20 ± 10 %) and rims (7 ± 9 %) were detected (**Fig. 6c**, **g**), arguing that these structures represent intermediate states during the formation of membrane cups. In conclusion, our in vivo experiments demonstrated that membrane remodeling by ATG16L1 variants that we revealed from reconstitutions in vitro are reproduced on cellular membranes in vivo. Moreover, variants ATG16L1^{230} and ATG16L1^{264} are impaired in cup formation while variants ATG16L1^{307} and ATG16L1^{WT} promote the formation of expanded cups and autophagosome-like vesicles, arguing that while the AIR and coiled coil domains of ATG16L1 are required for cup formation, they are not sufficient but need support from the C-terminal membrane binding region of ATG16L1.

Having established the contribution of ATG16L1 in cup formation, we next focused on LC3B. We therefore performed CLEM-PREM experiments of cells in which LC3B was knocked down (**Extended Data Fig. 5e**). As expected, WIPI2-CAAX efficiently recruited ATG16L1 to the PM. However, we only observed amorphous membrane protrusions. Characteristic structures, including rims, cups or autophagosome-like vesicles, were not observed. To exclude, that cup-

formation depends on overexpression of LC3B, we also performed PREM-CLEM experiments in cells expressing endogenous LC3B. We found that membrane cups are formed, although the frequency was much lower than in cells that overexpressed LC3B. Moreover, endogenous LC3B strongly colocalized with membrane cups (**Extended Data Fig. 5f**), demonstrating that endogenous LC3B promotes cup formation. This observation is significant because it reveals that LC3B is required for cup formation while other ATG8 family members cannot compensate loss of LC3B. We next tested whether LC3B is also sufficient for cup formation. We therefore performed PREM experiments in cells expressing WIPI2-CAAX and ATG16L1 but lacking all ATG8 homologs (Hexa-KO cells). Consistent with the requirement of LC3B for cup formation, no membrane cups were observed (**Extended Data Fig. 5g**). However, co-expression of LC3B in these cells restored the formation of membrane cups (**Extended Data Fig. 5h**). This result demonstrates that LC3B is required and sufficient for cup formation in vivo and that other ATG8 homologs are not participating in the process. In conclusion, our data showed that cup formation requires a coordinated action involving LC3B and ATG16L1.

Function of ATG16L1 in nonselective autophagy

The formation of membrane cups is a hallmark of nonselective autophagy and our data suggests that this process is driven by LC3B and ATG16L1. To test this hypothesis, we studied the autophagic activity of the different ATG16L1 variants that we already characterized in our reconstitution approaches. We first determined the E3-ligase activity of the different ATG12–ATG5-ATG16L1 complexes. We found that ATG16L1 variants that lacked the WIPI2 binding site ($ATG16L1^{NT}$ and $ATG16L1^{207}$) did not promote LC3B conjugation in ATG16L1 KO cells, while $ATG16L1^{230}$, $ATG16L1^{264}$, $ATG16L1^{307}$ and $ATG16L1^{FL}$ fully restored lipidation in vivo (**Extended Data Fig. 6a**).

We further tested whether the deletion of membrane binding domains in ATG16L1 affects its subcellular localization. We therefore compared levels of ATG16L1 variants in cytosolic and membrane fractions of ATG16L1 KO cells. Consistent with in vitro data from a previous study[30], $ATG16L1^{307}$ and $ATG16L1^{FL}$ were enriched in membrane fractions, while membrane binding was strongly impaired for ATG16L1 variants in which the C-terminal membrane binding region was

(partially) deleted (**Extended Data Fig. 6b**). Furthermore, ATG16L1^{307} and ATG16L1^{FL} were detected at large ring-like structures (**Extended Data Fig. 6c**, **d**) whereas ATG16L1^{230} and ATG16L1^{264} formed much smaller puncta (**Extended Data Fig. 6c**, **e**). To reveal the nature of these ATG16L1 puncta, we determined their ultrastructure by correlative light and transmission electron microscopy (CLEM). Large ATG16L1 puncta in ATG16L1^{307} expressing ATG16L1 KO cells corresponded to complete autophagosomes while the majority of ATG16L1 puncta in KO cells that expressed ATG16L1^{230} or ATG16L1^{264} colocalized with ER or mitochondria (**Fig. 7a**, **b**). Moreover, all ATG16L1 variants were found on clusters of small vesicles which are most likely involved in the formation of the previously described HyPas[34] (**Fig. 7b**, **Movie S9** and **Extended Data Fig. 6f**). CLEM is very well suited to investigate the subcellular localization of proteins, but the method suffers from limited preservation of membranes and does not provide information on three dimensions. To overcome this limitation, we applied two complementary techniques to characterize the morphology of organelles and membranes in cells expressing ATG16L1^{230} and ATG16L1^{307}. We first used focused-ion beam scanning electron microscopy (FIB-SEM) to obtain structural information on the entire 3-dimensional volume of the cell. We observed a strong accumulation of phagophores, autophagosomes and autolysosomes in cells expressing ATG16L1^{307} (**Fig. 7c**, **Movie S10**). This is consistent with our observation that ATG16L1^{307} forms big puncta in cells and promotes cup formation in vitro and in vivo. By contrast, no phagophores or autophagosomes were detected in cells expressing ATG16L1^{230}. Instead, we detected unusual, deformed membrane structures (**Fig. 7d**, **Movie S11**). We characterized these structures in more detail using serial sectioning EM, in which membranes are better preserved than in FIB-SEM. A strong accumulation of phagophores and autophagosomes was observed in ATG16L1 KO cells expressing ATG16^{FL} or ATG16L1^{307} (**Extended Data Fig. 7a, b**). By contrast, deformed double-membrane structures were observed in cells expressing ATG16L1^{230} which correspond to unusual membrane structures in FIB-SEM micrographs (**Extended Data Fig. 7c**).

We next performed autophagic flux analysis using stable cell lines that express ATG16L1 variants at native levels using GFP-RFP-LC3B. We found that complementation of ATG16L1 KO cells by expression of ATG16L1^{FL} at native levels restored autophagic flux. The same was true for cells that expressed ATG16L1^{307}, which was unimpaired in cup formation in vitro and in vivo. However, autophagic flux was abrogated in cells that expressed ATG16L1^{230} or ATG16L1^{260}

(**Extended Data Fig. 7d, e**). Our results thus show that ATG16L1 variants that promote the formation of membrane cups in vitro and in vitro also promote the formation of autophagosomes in nonselective autophagy, while variants that are impaired in cup formation are also impaired in autophagy.

Consistent with expectation, we observed a strong induction of autophagic flux upon starvation while Bafilomycin treatment inhibited or abrogated flux (**Extended Data Fig. 7d, e**).

Taken together, we observed a strong correlation between cup-formation in reconstitutions and formation of autophagosomes in cells. ATG16L1 variants that deform membranes into mature cups also promote the formation of autophagosomes, while autophagy was inhibited in cells expressing variants that were impaired in cup formation.

Discussion

The conjugation of ATG8 proteins to phagophore membranes by an Ub-like conjugation system is a key step during the formation of autophagosomes. LC3B and its E3-ligase complex promote phagophore expansion and the high abundance of LC3B on phagophore membranes has made LC3B a widely used marker for autophagosomes in nonselective autophagy[25,35]. Moreover, the E3-ligase complex remains associated with phagophores throughout expansion, but its subunits ATG16L1 and ATG5 are exclusively targeted to their outer membrane[36,37], suggesting that the complex itself exhibit an asymmetric distribution on phagophores. Although, recent studies showed that LC3 proteins and components of the Ub-like conjugation machinery are not essential for the formation of autophagosomes[21,22,24], elongated, unclosed phagophores accumulate in cells lacking components of the conjugation machinery[38,39]. All these data provide plenty of evidence that LC3 proteins, and the E3-ligase complex in particular, are important for phagophore expansion. However, the underlying molecular mechanisms remain to be established.

Here, we investigated how LC3B and ATG12–ATG5-ATG16L1 remodel membranes in vitro and in vivo by reconstituting the conjugation of LC3B to model membranes and to the PM of cells. We found that ATG12–ATG5-ATG16L1 assembles with LC3B into membrane coats that cover extended areas of flat and curved membranes in vitro and in vivo. Furthermore, LC3B and ATG12–ATG5-ATG16L1 deform flat membranes into cups that share remarkable similarities with

phagophores. The formation of membrane cups was strictly dependent on the capacity of ATG16L1 to form membrane coats. Fully expanded membrane cups were only induced by ATG16L1 variants that assembled with LC3B and ATG12–ATG5 into flat scaffolds that covered extended membrane areas in vitro and in vivo (ATG16L1^{307}, ATG16L1^{FL}). The variant ATG16L1^{264} formed loose scaffolds and deformed membranes into flat cup-like profiles, while ATG16L1^{230}, which did not promote scaffold formation, induced only membrane protrusions with ring-like morphology. Interestingly, membrane rings and flat cups were also found in reconstitutions with ATG16L1^{FL} (**Fig. 7f**), suggesting that ATG16L1^{230} and ATG16L1^{264} stabilize intermediate states of cup formation (**Fig. 7f** and **Movie S12**).

The combination of our two reconstitution systems allowed us for the first time to untangle the contribution of ATG16L1 and LC3B in membrane remodeling at a molecular level. Immuno-gold electron microscopy and 3D-STORM revealed that ATG16L1 is present on highly curved membranes in vivo. Moreover, our CLEM-PREM data demonstrated that ATG16L1 colocalized with membrane protrusions and membrane rims in areas devoid of LC3B and in cells depleted of LC3B by siRNA, indicating that ATG16L1 induces and stabilizes positive membrane curvature independently of LC3B. This observation is consistent with previous reports showing that ATG16L1 possesses several membrane binding sites and interacts preferentially with negatively charged membranes[30,31,40]. We found that a sustained interaction of ATG16L1 with model membranes containing moderate levels of negatively charged lipids was LC3B dependent. Moreover, expanded membrane cups were only observed in reconstitutions with ATG16L1^{307} and ATG16L1^{FL}, while ATG16L1^{264} and ATG16L1^{230} induced the formation of premature cups and flat rim-like structures. This demonstrates that the C-terminal membrane binding domain that connect coiled coil and WD domains of ATG16L1 is indispensable for cup formation. Interestingly, a previous study reported that this membrane binding region is required for autophagy[30], suggesting that the processes of cup formation and nonselective autophagy are related. In support of this notion, we found that the propensity of ATG16L1 variants to induce membrane cups correlates with their autophagic activity. Large volumetric electron microscopy showed that cells expressing ATG16L1^{230} were devoid of phagophores, autophagosomes and autolysosomes. Moreover, autophagy flux was inhibited in cells expressing ATG16L1^{230} and ATG16L1^{264}. By contrast, expression of ATG16L1^{307}, which contained the C-terminal membrane binding region,

restored autophagic flux in ATG16L1 KO cells as well as the formation of phagophores, autophagosomes and autolysosomes, as evident from FIB-SEM and serial sectioning TEM experiments. Taken together, we provide compelling evidence that the C-terminal membrane binding domain of ATG16L1 is required for cup expansion and the biogenesis of nonselective autophagosomes.

Even though ATG16L1 drives membrane remodeling and cup formation, our PREM-CLEM experiments demonstrated that cup formation also depends on LC3B. In cells expressing ATG16L1^{FL} and LC3B, cups only emerged in regions where both proteins colocalized while no cups were detected in cells depleted of LC3B. Interestingly, a recent study showed that the N-terminus of LC3B is inserted into the membrane in cis[41], suggesting that membrane insertion promotes cup formation. The fact that no cups are present in LC3B depleted cells and that complementation of HexaKO cells by LC3B restores cup formation demonstrates that other ATG8 proteins cannot compensate for LC3B and that LC3B is required and sufficient for cup formation. To our knowledge, this is the first example of a process that strictly depends on LC3B.

But why does ATG16L1 behave differently depending on its interaction with LC3B? A previous study demonstrated that ATG3 contains an amphipathic helix and senses positive membrane curvature, suggesting that lipidation of LC3B occurs at highly curved membrane regions[42]. Consistent with this study, we found that ATG16L1 induces membrane deformations independently of LC3B, suggesting that the local formation of high membrane curvature by ATG16L1 promotes the recruitment of ATG3-LC3B conjugates to membranes to induce lipidation of LC3B.

Taken together, our data reveal that the recruitment of ATG16L1 to membranes induces the formation of positive membrane curvature and rim-like structures (**Fig. 7f** and **Supplemental Movie 12**). The expansion of these structures into cups depends on the formation of membrane coats comprising LC3B and ATG12–ATG5-ATG16L1 on the shallow curved face of cups (**Fig. 5d** and **7f**), which would also explain why ATG5 and ATG16L1 are asymmetrically distributed on phagophores[37].

In nonselective autophagy, phagophores are formed at omegasomes, which are specialized domains of the ER, and their expansion involves mobilization of various lipid sources and direct transfer of lipids from the ER[43]. The relationship between phagophores and

omegasomes remains controversial, but electron microscopy data suggested that phagophore emerge from omegasomes[44,45], requiring a remodeling reaction that extrude membrane cups from a donor membrane, as we observed in our reconstitutions in vitro and in vivo (**Fig. 7e**).

Other studies suggest that phagophores are nucleated by ATG9 vesicles de novo near omegasomes[6,46] and their expansion involves direct lipid transfer from the ER by ATG2[47,48], redistribution of lipids to the inner membrane of phagophores by ATG9[49,50], and vesicular transport from various other sources[43]. Although in such a scenario phagophore extrusion is not required, the precursor needs to be shaped to generate a membrane cup, which involves similar mechanisms (**Fig. 7e**).

Independently of the nature of phagophore precursors, their expansion requires a massive mobilization of lipids that are provided by lipid transfer from the ER and vesicular transport from various organelles. We provide compelling evidence that LC3B and ATG16L1 collaborate to promote phagophore expansion by shaping membrane precursors into cups, providing a unified model of phagophore formation and expansion in nonselective autophagy.

Acknowledgements

We thank Frank Lafont and Sebastien Janel (Center for Infection and Immunity of Lille, Institut Pasteur de Lille, Lille, France) for access to atomic force microscopes, scientific and technical support and fruitful discussions. We thank Alexis Canette (Institut de Biologie Paris-Seine (IBPS) Electron Microscopy facility) for help with metal coaters and Jeanne Lainé (Sorbonne Université, INSERM, Institut de Myologie) for her expertise in preparing thin sections for EM. We also thank Sharon Tooze (The Francis Crick Institute, London, UK) for the WIPI2-CAAX construct and fruitful discussions. We thank Michael Lazarou (Monash University, Melbourne) for sharing his HexaKO cells. Australia We thank Anastasia Gazi, Olivier Gorgette and Gérard Pehau-Arnaudet of the Ultrastructural BioImaging Platform (UTechS UBI, Institut Pasteur Paris) for access to electron microscopy and sample preparation equipment as well as for technical support and training. We thank Jacomina Krijnse Locker (Paul-Ehrlich-Institut and formerly at the Institut Pasteur Paris) for helpful discussions and support. We thank Arnaud Echard and Chiara Zurzolo (Institut Pasteur, Paris) for commenting on the manuscript. UTechS PBI is part of the France–BioImaging infrastructure network (FBI) supported by the French National Research Agency (ANR-10-INBS-

04; Investments for the Future), and acknowledges support from Institut Pasteur, ANR/FBI, the Région Ile-de-France (grant on infectious diseases DIM1HEALTH), and the French Government Investissement d'Avenir Programme—Laboratoire d'Excellence 'Integrative Biology of Emerging Infectious Diseases' (ANR-10-LABX-62-IBEID) for the use of ELYRA7 microscope (Carl Zeiss). We are grateful for support of Adeline Mallet (UBI) and financial support for UBI equipment from the French Government Programme Investissements d'Avenir France BioImaging (FBI, N° ANR-10-INSB-04-01) and the French gouvernement (Agence Nationale de la Recherche) Investissement d'Avenir programme, Laboratoire d'Excellence "Integrative Biology of Emerging Infectious Diseases" (ANR-10-LABX-62-IBEID). This work was supported by the ERC-Starting Grant GA 638603 (Autophagy in vitro), by the Agence Nationale de la Recherche (grants ANR-22-CE13-0007-01, AUTOBEND) and by intramural funds of the Institut Pasteur to TW; by Sorbonne Université, INSERM, Association Institut de Myologie core funding and the Agence Nationale de la Recherche (grants ANR-20-CE13-0024-02 and ANR-21-CE13-0018-01) to SV.

Author contribution

JM purified proteins, did all in vitro reconstitutions, performed FRAP and AFM experiments, performed autophagy experiments (ATG16L1 puncta, membrane binding, LC3B conjugation), generated ATG16L1 truncates and prepared samples for PREM (in vitro and in vivo). SBM generated constructs, performed confocal imaging of ATG16L1 plasma membrane targeting, provided samples for in vivo PREM studies and performed CLEM-PREM, CGB performed TEM and CLEM experiments including segmentation and quantification. SV conceptualized, performed and analyzed all PREM experiments, acquired funding and co-supervised SBM. DC performed colocalization experiments with ATG14, ATG9, Ulk1, autophagy inhibition and siRNA experiments with support by CN. SB generated stable cell lines and performed flux experiments, SR performed in vivo characterization of ATG16L1 variants together with JM, AS performed 3D-STORM experiments and EP and CGB performed FIB-SEM and serial sectioning TEM experiments. TW conceptualized, supervised and administrated the study, analyzed data, wrote the manuscript draft, provided resources and acquired funding. All authors analyzed and discussed their results and revised the manuscript.

Declaration of Interests

The authors declare no competing interests.

Figure Legends

Fig. 1: Conjugation of LC3B to model membranes in vitro.

Alexa 488 labeled LC3B^{G120} was conjugated to fluorescent labeled Giant Unilamellar Vesicles (**a**-**c**, **e**-**f**) (GUVs, red) or to supported lipid bilayers (SLBs, **d**) in the presence of unlabeled ATG16L1^{FL} (**b, c, d**) or ATG16L1^{NT} (**e**) as illustrated by the cartoon (**a**). Images show conjugation at indicated timepoints.

(**b**) Arrowheads indicate membrane deformation. Kymographs are derived from the area depicted by the white line.

(**c**) 3D reconstruction of the GUV shown in (**b**) from a z-stack recorded at the end of the conjugation.

(**f**) FRAP experiment of a GUV (red) to which LC3B$^{G120,\ Atto590}$ was conjugated in the presence of ATG16L1^{Alexa488}. The fluorescence was bleached in the indicated area (arrowhead) and recovery is shown seven minutes after bleaching (see also **Extended Data Fig. 1c)**. Scale bars = 10µm.

Fig. 2: Scaffold formation by LC3B and ATG12–ATG5-ATG16L1 on model membranes in vitro.

(**a**) Atomic Force Microscopy height profile (with colors defined in corresponding scales) of a supported lipid bilayer on plasma cleaned glass.

(**b**) Similar height profiles after LC3B^{G120} conjugation with the Ub-like conjugation machinery including ATG16L1. Scale bars = 500 nm. The dotted red lines in the plot were taken from the area indicated by the white line in the height profile. The two lines indicate the membrane height (set to zero) and the average protein height used to calculate the thickness of the protein coat. The height profile was averaged and a Gaussian filter was applied for better visualization.

(**c**) Height profile of an SLB to which LC3B was conjugated in the presence of ATG16L1^{NT}. The colors correspond to heights as indicated by the corresponding color scales. Scale bar = 2 µm.

(**d**) The cartoon shows the domain architecture of ATG16L1 and highlights domain borders used to generate ATG16L1 truncations.

(**e**) Quantification of FRAP experiments (shown in **Extended Data Fig. 2b**) of ATG16L1 variants as indicated. The solid line shows the exponential fit of experimental data (dots).

(**f**) The chart shows the average mobile fractions from evaluations as shown in (**e**) from corresponding FRAP experiments shown in **Extended Data Fig. 2b**.

Fig. 3: Cup formation by ATG16L1 on SLBs in vitro.

(**a, c**-**e**) High magnification PREM views of SLB to which LC3B was conjugated in the presence of ATG16L1^{FL} (**a**), ATG16L1^{Nt} (**c**), ATG16L1^{307} (**d**), ATG16L1^{264} (**e**)**,** ATG16L1^{230} (**f**) and ATG16L1^{207} (**g**).

(**b**) Quantification of membrane deformations on SLBs in reconstitution reactions with ATG16L1 variants. The chart show fractions of membrane deformations represented as mean ± SD from 150 structures for each variant. N=4 experiments, statistical significance was calculated by a two-tailored T-Test with p-values (compared to ATG16L1) for 307: 0.4, 0.002, 0.002; 264: 4E-09, 2E-07, 0.0005; 230: 5E-10, 1E-06, 2E-07; 207: 2E-10, 0.005, 3E-07. Scale bars = 1 µm (overview, top panels - general appearance of SLBs), and 100 nm (insets). The diameter of membrane rims is 15-20 nm for ATG16L1 (**a**), 10-15 nm for ATG16L1^{264} (**e**), and 15-50 nm for ATG16L1^{230} (**f**).

Fig. 4: WIPI2-CAAX recruits ATG16L1 and LC3B to the plasma membrane independently of the upstream autophagy core machinery.

(**a**) Scheme representing the experimental outline and confocal image of HeLa cells co-expressing WIPI2-CAAX, GFP-LC3B and mCherry-ATG16L1. Scale bar = 10 µm.

(**b**) Confocal images of HeLa cells expressing WIPI2-CAAX, ATG16L1, GFP-LC3B and either mKate-ATG14, ULK1, or RFP-ATG9 as indicated. mKate and RFP were stained using an anti-RFP primary and an Alexa 594 secondary antibody and DAPI (nuclei, blue). ULK1 was stained using an anti-ULK1 primary and an Alexa 647 secondary antibody and DAPI (nuclei, blue). For each experiment, a ROI was drawn for each cell and the Pearson's coefficient (R) for colocalization of GFP-LC3B with either ULK1, ATG14 or ATG9 was calculated after background subtraction. For each condition, a colocalization map is shown. The association of LC3B with either ATG14, ULK1 or ATG9 was representatively shown with Colocalization Colormap tool, where normalized mean deviation product (nMDP) shows the correlation between intensities of corresponding pixels. Scale bars = 10 µm. Results are represented as mean ± SD and a one-way ANOVA followed by

Holm-Sidak post hoc test was used to evaluate statistical significance with ***p < 0.001 (ATG14: N=5, n=46; ULK1: N=3, n=48; ATG9: N=3, n=33). See also **Extended Data Fig. 3a**.

(**c**) Confocal images showing targeting of LC3B to the PM in HeLa cells transfected with scrambled siRNAs (siCont) or siRNA against ULK1 or ATG14 and expressing mCherry-WIPI2-CAAX and 3xHA-LC3B. 3xHA-LC3B was stained using an anti-HA primary and an Alexa 488 secondary antibody and DAPI (nuclei, blue). Quantifications show the percentage of LC3B puncta at the PM after background subtraction. Magnification per each siRNA is shown on the right. The total number of LC3B puncta was first calculated per cell and thereafter the number of LC3B puncta at the plasma membrane was calculated in an ROI 1.5-µm width from the plasma membrane using ComDet plug-in of Fiji software. Data are expressed as mean ± SD of N = 3 independent experiments with n_{siCont} = 126 cells; n_{siULK1} = 124 cells; $n_{siATG14}$ = 118 cells. Scale bars = 10 µm. Statistical significance was evaluated with a one-way ANOVA followed by Dunnett post hoc test. ns: no significance. See also **Extended Data Fig. 3b**.

(**d**) Confocal images showing targeting of LC3B to the PM in starved HeLa cells expressing mCherry-WIPI2-CAAX and 3xHA-LC3B and treated with either DMSO (control), the ULK1 kinase inhibitor SBI-0206965 or the PI3 kinase inhibitor SAR405. 3xHA-LC3B was stained using an anti-HA primary and an Alexa 488 secondary antibody and DAPI (nuclei, blue). Left graphic: The total number of LC3B puncta per mm^2 was first calculated to ensure proper inhibition of early stages of autophagy by the inhibitors. Right graphic: Quantification was performed as in (**c**). Magnification per each inhibitor is shown in the right. ComDet plug-in of Fiji software was used. Scale bars = 10 µm. Data are shown as mean ± SD from N = 3 independent experiments; n_{DMSO}= 131 cells; n_{SAR405}= 113 cells; $n_{SBI\text{-}0206965}$ = 113 cells. Statistical significance was evaluated with a one-way ANOVA followed by Sidak post hoc test with ***p < 0.001 and ns: no significance.

(**e**) Confocal images showing targeting of LC3B to the PM in HeLa cells in FED (0h) and after 1h, 2h or 3h starvation. HeLa cells expressing mCherry-WIPI2-CAAX and 3xHA-LC3B. 3xHA-LC3B was stained using an anti-HA primary and an Alexa 488 secondary antibody and DAPI (nuclei, blue). Upper and Lower graphics: Quantification was performed as in (**d**), respectively and magnification per each time point is shown in the lower panel. Scale bars = 10 µm. Data are shown as mean ± SD from N = 3 independent experiments; n_{T0}= 94 cells; n_{1h}= 81 cells; n_{2h} = 114

cells and n_{3h} = 107 cells. Statistical significance was evaluated with a one-way ANOVA followed by Dunnett post hoc test with ***p < 0.001 and ns: no significance.

Fig. 5: Reconstitution of membrane remodelling and cup formation at the plasma membrane.

(**a**, **b**, **c**) The schematic drawing outlines the experimental strategy to induce the lipidation of LC3B to the plasma membrane of cells. Images in **a, b** and **c** show high magnification views of unroofed ATG16L1 knock out HeLa cells transfected with WIPI2-CAAX, scale bar = 200 nm (**a**), WIPI2-CAAX and ATG16L1, scale bar = 200nm (**b**) and WIPI2-CAAX, ATG16L1 and LC3B, scale bar = 500 nm (**c**).

(**d**) High magnification PREM images of unroofed HeLa cells expressing WIPI2-CAAX, HA-ATG16L1 and GFP-LC3B and immuno-gold labelled (yellow) for GFP and HA as indicated. Scale bars = 500 nm (overviews) and 100 nm (insets).

Fig. 6: Generation of membrane cups by LC3B and ATG12–ATG5-ATG16L1 in vivo.

(**a**) 3D-STORM image showing the special distribution of ATG16L1 at the plasma membrane in an ATG16L1 knock out cell expressing WIPI2-CAAX, HA-ATG16L1 (immunolabeled using anti-HA and Alexa647 conjugated secondary antibody) and LC3B. Top and side views as indicated by the coordinates. Inset shows a higher magnification image of the area indicated by the white rectangle. Scale bars of overviews = 2 µm and of insets = 0.5 µm.

(**b**) Correlative SMLM and PREM image of an unroofed cell expressing WIPI2-CAAX, HA-ATG16L1 (red) and LC3B (green). Inset shows the area indicated by the white rectangle at higher magnification. Scale bar of overview = 10 µm and of inset = 0.5 µm. See also **Extended Data Fig. 5a** and **b**.

(**c**) Bar chart represents mean ± SD of the fraction of membrane deformations classified as autophagic vesicles, expanded cups, premature cups, or rims in independent experiments with a total of n > 100 structures for each ATG16L1 variant. Statistical significance was calculated using unpaired two-tailed Student's t-tests with * P ≤ 0.1, ** P ≤ 0.05, *** P ≤ 0.005.

(**d**-**g**) Confocal images of ATG16L1 KO cells expressing WIPI2-CAAX, GFP-LC3B and mCherry-tagged $ATG16L1^{230}$ (**d**), $ATG16L1^{264}$ (**e**), $ATG16L1^{307}$ (**f**) and $ATG16L1^{FL}$ (**g**). Merged GFP (green) and mCherry (red) images are shown. Confocal images of the corresponding single channels are

shown in **Extended Data Fig. 5d**. Scale bar = 5µm. The high magnification PREM views show characteristic membrane deformations of unroofed ATG16L1 KO cells expressing WIPI2-CAAX, LC3B and HA-ATG16L1 variants as indicated. Scale bars = 1 µm and 200 nm (insets).

Fig. 7: Localization of ATG16L1 variants at cellular membranes revealed by CLEM.

(**a**) Correlative light electron microscopy images of cells expressing HA-tagged ATG16L1^{307} ATG16L1^{264} or ATG16L1^{230} in ATG16L1 knock out cells, labeled with anti-HA primary and Alexa488 labeled secondary antibodies. Scale bars = 1 µm (overviews) and 100 nm (insets). See also **Extended Data Fig. 6f**.

(**b**) Histogram shows relative abundance of ATG16L1 positive and autophagic structures (indicated by the legend) from CLEM images (as shown in **a**) of five cells with similar surface. Data represent fractions of at least 20 structures, normalized to 100 %.

(**c**, **d**) Correlative large volume focused ion beam-scanning electron microscopy (FIB-SEM) of a cell expressing HA-tagged ATG16L1^{307} (**c**) and ATG16L1^{230} (**d**). One representative slice of the entire cellular volume is shown. The complete data set is presented in Movies S10 and S11. Scale bars = 200 nm (overviews) and 50 nm (insets). AL = autolysosome, AP = autophagosome, Ph = phagophore, M = mitochondria, N = nucleus, ER = endoplasmic reticulum, VC = vesicular cluster.

(**e**) Model of cup formation in autophagy. Two scenarios are shown: (i) remodeling of a precursor membrane into a membrane cup and (ii) extrusion of cups from an existing membrane. Both scenarios involve similar membrane remodeling events, including induction of positive membrane curvature by ATG16L1 (bending), and cup expansion by the formation of membrane coats containing LC3B and ATG12–ATG5-ATG16L1 (scaffolding).

(**f**) Comparison of endpoints of cup formation as shown in high magnification PREM views of unroofed ATG16L1 KO cells expressing WIPI2-CAAX, LC3B and HA-ATG16L1^{230}, HA-ATG16L1^{264}, HA-ATG16L1^{307} and HA-ATG16L1^{FL} (left panel, scale bars = 1 µm) with intermediate of cup formation in PREM views of ATG16L1 KO cells expressing WIPI2-CAAX, LC3B and HA-ATG16L1^{FL} (right penal, scale bars = 500 nm).

Methods

Reagents and Resources

REAGENT or RESOURCE	SOURCE	IDENTIFIER

Antibodies		
Rabbit monoclonal anti-HA	Cell Signaling Technology	Cat#3724S; RRID: AB_1549585
Mouse monoclonal anti-HA	Santa Cruz Biotechnology	Cat#sc-7392; RRID: AB_627809
Mouse monoclonal anti-ATG16L1	MBL International	Cat#M150-3; RRID: AB_1278758
Rabbit monoclonal anti-LC3B	Cell Signaling Technology	Cat#3868S; RRID: AB_2137707
Rabbit polyclonal anti-LC3B	MBL International	Cat#PM036; RRID: AB_2274121
Rabbit monoclonal anti-GAPDH	Cell Signaling Technology	Cat#5174S; RRID: AB_10622025
Mouse monoclonal anti-WIPI2	Abcam	Cat#ab105459; RRID: AB_10860881
Rabbit polyclonal anti-GFP	Molecular Probes	Cat#A6455; RRID: AB_221570
Mouse monoclonal anti-beta actin	Thermo Fisher Scientific	Cat#MA1-140; RRID: AB_2536844
Rabbit polyclonal anti-ATG14	Cell Signaling Technology	Cat#5504; RRID: AB_10695397
Rabbit polyclonal anti-RFP	Thermo Fisher Scientific	Cat#R10367; RRID: AB_10563941
Rabbit monoclonal anti-ULK1	Cell Signaling Technology	Cat#8054; RRID: AB_11178668
Mouse monoclonal anti-ULK1	Santa Cruz Biotechnology	Cat#sc-390904; RRID: AB_2861148
Goat polyclonal anti-rabbit Alexa Fluor 488	Thermo Fisher Scientific	Cat#A11034; RRID: AB_2576217
Goat polyclonal anti-rabbit Alexa Fluor 594	Thermo Fisher Scientific	Cat#A11037; RRID: AB_2534095
Goat polyclonal anti-mouse Alexa Fluor 647	Molecular Probes	Cat#A21235; RRID: AB_2535804
Rabbit polyclonal anti-GFP, conjugated to gold nanobeads	Thermo Fisher Scientific	Cat#A11122; RRID: AB_221569
Goat anti rabbit, conjugated to gold nanobeads	Aurion	Cat#815.011
Bacterial and virus strains		
E.coli K12, Top10	Thermo Fisher Scientific	Cat#C404010
E.coli K12, Rosetta	Sigma-Aldrich	Cat#70954
Chemicals, peptides, and recombinant proteins		
1,2-dioleoyl-sn-glycero-3-phosphoethanolamine (DOPE,18:1)	Avanti Polar Lipids	Ref no: 850725
1,2-dioleoyl-sn-glycero-3-phosphocholine (DOPC,18:1)	Avanti Polar Lipids	Ref no: 850375
1-palmitoyl-2-oleoyl-sn-glycero-L-serine Avanti Polar Lipids (POPS,16:0-18:1)	Avanti Polar Lipids	Ref no: 840034
Cholesterol	Avanti Polar Lipids	Ref no: 700000
Lissamine rhodamine PE	Avanti Polar Lipids	Ref no: 810158
Dulbecco's Modified Eagle Medium (DMEM)	Gibco	Ref no: 31966-021
Earle's Balanced Salt Solution (EBSS)	Gibco	Ref no: 15140-122
Opti-MEM	Gibco	Ref no: 31985-062
Trans IT-HeLa MONSTER Transfection Kit	Mirus	Cat#MIR2900
Cellfectin-II	Thermo Fischer Scientific	Ref no: 10362100
SAR405	Ape Bio	Cat#A8883
SBI-0206965	Sigma Aldrich	Ref no: SML1540
Complete protease inhibitor cocktail	MERCK - roche	Ref no: 11697498001
Super signal West Pico chemiluminescent substrate	Thermo Fischer Scientific	Ref no: 34577
Alexa Fluor 488 C5 Malemide	Thermo Fischer Scientific	Ref no: A10254
Atto590	ATTO-TEC	Ref no: AD590
Cryo ultramicrotome sample pin	Thermo Fischer Scientific	Ref no: 75959-06
CRYO IM Diamond knife	neobits	DCIMM3530
Fomvar/carbon-coated copper finder grids Cu HF15	Oxford instruments	#AGG245
DiATOME trim 45	Labtech-em.com	#DTB45
LC3A	Wetzel et al, 2020	N/A
LC3B	Wetzel et al, 2020	N/A
Cys-LC3B	This study	N/A
ATG7	Wetzel et al, 2020	N/A

ATG3	Wetzel et al, 2020	N/A
ATG12-ATG5	Wetzel et al, 2020	N/A
ATG16L1 (Full length)	This study	N/A
ATG16L1 (1-307)	This study	N/A
ATG16L1 (1-264)	This study	N/A
ATG16L1 (1-230)	This study	N/A
ATG16L1 (1-207)	This study	N/A
ATG16L1 (11-43)	This study	N/A
Experimental models: Cell lines		
Human: HeLa	Cell Lines Service	Cat#300194
Oligonucleotides		
siRNA targeting sequence: ULK1	Thermo Fisher Scientific	Cat#4457308
siRNA targeting sequence: ATG14	Thermo Fisher Scientific	Cat#4392420
Primers list, see table S2	This paper	N/A
Recombinant DNA		
Plasmid: Wipi2b FTTG CAAX	Sharoon Tooze Lab	Dooley et al; 2014
Plasmid: mCherry-wipi2b FTTG CAAX	Sharoon Tooze Lab	Dooley et al; 2014
Plasmid: 3HA ATG16L1 (Full Length)	This study	N/A
Plasmid: 3HA ATG16L1 (Full Length)	This study	N/A
Plasmid: 3HA ATG16L1 (1-307)	This study	N/A
Plasmid: 3HA ATG16L1 (1-264)	This study	N/A
Plasmid: 3HA ATG16L1 (1-230)	This study	N/A
Plasmid: 3HA ATG16L1 (1-207)	This study	N/A
Plasmid: mCherry ATG16L1 (Full Length)	This study	N/A
Plasmid: mCherry ATG16L1 (1-307)	This study	N/A
Plasmid: mCherry ATG16L1 (1-264)	This study	N/A
Plasmid: mCherry ATG16L1 (1-230)	This study	N/A
Plasmid: mCherry ATG16L1 (1-207)	This study	N/A
Plasmid: mKate2-ATG14	This study	N/A
Plasmid: pUNO1-hULK1	InvivoGen	Cat#puno1- (gene)
Plasmid: RFP-ATG9	Sharoon Tooze Lab	N/A
Plasmid: GFP-LC3B	Wetzel et al, 2020	N/A
Software and algorithms		
ImageJ	ImageJ/Micro-manager (Edelstein *et al*. 2014)	https://fiji.sc/
GraphPad Prism 8.0.1	GraphPad	https://www.graphpad.com/scientific-software/prism/
Midas	IMOD (Kremer *et al*. 1996)	http://bio3d.colorado.edu/imod
Serial EM	serialEM MFC application version 1.0.0.1	http://bio3d.colorado.edu/SerialEM/
Amira	Thermo Fisher Scientific	https://www.thermofisher.com/fr/fr/home/industrial/electron-microscopy/electron-microscopy-instruments-workflow-solutions/3d-visualization-analysis-software/3d-visualization-analysis-software-resource-center/amira-avizo-software-system-requirements.html
Imod	IMOD (Kremer *et al*. 1996)	http://bio3d.colorado.edu/imod

Cells

HeLa cells were purchased from Cell Lines Service (# 300194) and cultured in DMEM (Gibco, #31966-021) containing 10 % FBS (Sigma-Aldrich, F4135), 100 U/ml penicillin and 100 µM streptomycin (Gibco, 15140-122) at 37°C in a 5 % CO_2 atmosphere. Starvation of HeLa cells was induced by washing them three times with DPBS and incubation for 2 h in presence of Earle's Balanced Salt Solution (EBSS, Sigma Aldrich, E2888). HeLa cells were transfected with TransIT-HeLaMONSTER Transfection Kit (Mirus, MIR2904) or using JetPRIME® (Polyplus 114-01) as per manufacturer's protocol and analyzed 24 h to 48 h post-transfection.

Insect cells

SF9 and H5 were cultured at $1x10^6$ cells/ml in EX-CELL 420 serum-free medium supplemented with 5 % Fetal Bovine Serum for SF9 cells. Fastbac vector containing ATG7 (pCoofy27) / ATG16L1 (pCoofy29) were transformed into DH10MultiBac cells and the generated bacmids were isolated by Nucleo Bond BAC 100 (MACHEREY-NAGEL#740579). Virus stock was generated by transfecting SF9 cells with Cellfectin II (TFS#10362100). Virus titers were determined using the Virocyt (Sartorius) to calculate the MOI and SF9 cells (ATG7) or H5 cells (ATG16L1) were infected with a MOI of 1.

Protein purification

Human ATG proteins were expressed as fusion proteins with N-terminal affinity tags as indicated in Table S2. LC3B was expressed as processed, conjugation-competent variant lacking its C-terminal propeptide (referred to as $LC3B^{G130}$). ATG12-ATG5 was expressed using a polycistronic vector harboring cDNAs of *ATG7*, *ATG10*, *ATG5* and His10-tagged *ATG12*. LC3B, ATG3, ATG12–ATG5 and ATG16 variants were produced in E.coli. Cells were grown at 37°C, 180 rpm until the OD_{600} reached 0.6. Expression was induced by adding 0.3 mM IPTG and cells were grown further for 3 h at 37°C or at 18°C overnight (ATG16 variants). *E. coli* cells were harvested by centrifugation at 4500 g for 10 minutes, resuspended in lysis buffer (100 mM Tris-HCl pH 8.0, 300 mM NaCl (500 mM for ATG16L1), 20 mM imidazole, 10 % glycerol, 5 mM beta-mercaptoethanol) supplemented with complete protease inhibitor cocktail (Sigma) and benzonase (Sigma). Cells were lysed using an Avestin Emulsiflex C3 (ATA Scientific).
ATG7 and $ATG16L1^{FL}$ (full-length) were expressed in SF9 and H5 cells, respectively, and grown to $1x10^6$ cells/ml in EX-CELL 420 serum-free medium supplemented with 5 % Fetal Bovine Serum for SF9 cells. Baculovirus-infected insect cells were added in a ratio of 1:4000 (ATG7) and 1:1000 (ATG16L1). Cultures were incubated for 72 h at 25°C and 85 rpm. Cells were harvested by centrifugation at 2000 g for 15 minutes, washed with Dulbecco's phosphate buffered saline (DPBS, Gibco), resuspended in lysis buffer (without beta-mercaptoethanol for ATG7) and lysed using a dounce homogenizer. Soluble fractions of all cell lysates were collected after centrifugation at 45000 g for 1 h and incubated with Ni-NTA agarose for 1 h at 4°C. Unbound proteins were removed by washing with wash buffer (50 mM Tris-HCl pH 8.0, 300 mM NaCl (500 mM for ATG16L1), 5 mM imidazole, 10 % glycerol, 5 mM beta-mercaptoethanol) and eluted using elution buffer (50 mM Tris-HCl pH 7.4, 300 mM NaCl (500 mM for ATG16L1), 500 mM imidazole, 10 % glycerol). Except for $ATG16L1^{11-43}$, the affinity tags were removed by Prescission protease treatment for 45 min at room temperature in presence of 5 mM DTT (AppliChem) and 1 mM EDTA (Carl Roth). The His-MBP tag of $ATG16L1^{11-43}$ was cleaved by Prescission protease treatment in presence of ATG12-ATG5. The digested proteins were subjected to size exclusion chromatography on HiLoad 16/60 Superdex 75 (ATG3, LC3B and ATG16L1 variants) or Superdex 200 (ATG12-ATG5, ATG7, ATG16L1) columns, equilibrated with SEC buffer (25 mM Tris-HCl pH 7.4, 275 mM NaCl or 400 mM for ATG16L1) using an ÄKTA explorer (GE healthcare). The elution fractions containing protein of interest were pooled, concentrated and aliquots were flash frozen in liquid nitrogen and stored at -80°C. Protein quality and integrity of the ATG12-ATG5-$ATG16L1^{11-43}$ complex were characterized by SDS-PAGE and mass spectrometry.

Fluorescent labelling of proteins

Fluorescent labeling of proteins was performed using maleimide-coupling chemistry. Alexa Fluor 488 C_5 (Molecular Probes) was conjugated to an introduced N-terminal cysteine of LC3B while Atto590 (ATTO-TEC) was conjugated to

native cysteine residues in ATG16L1. Purified proteins were incubated with an equimolar amount of fluorescent dyes for 1 hr at room-temperature. Unbound dyes were removed by using HiTrap Desalting columns (GE healthcare, for LC3B), or Zeba Spin Desalting Columns (Thermo scientific, for ATG16L1). Labelling efficiency was determined spectroscopically.

Model membranes

Giant Unilamellar Vesicles (GUVs) were generated by electroformation on idium-tin oxide coated glass slides in custom made teflon chambers[51]. The lipid mixture consisting of 1,2-dioleoyl-sn-glycero-3-phosphoethanolamine (DOPE,18:1 PE, 40 mol%), 1,2-dioleoyl-sn-glycero-3-phosphocholine (DOPC,18:1 PC, 40 mol%), 1-palmitoyl-2-oleoyl-sn-glycero-L-serine (POPS,16:0-18:1 PS, 10 mol%), cholesterol (10 mol%) and lissamine rhodamine PE (0.1 mol%) was deposited on slides and dried in vacuum for 60 minutes. The assembled chamber was filled with 600 mOsM sucrose solution an alternating electric current (2 V, 10 Hz) was applied for 1.5 h. Detachment of GUVs was induced by reducing the current frequency to 2 Hz for 30 min. GUVs were diluted 1:1 with 600 mOsM sucrose solution and used immediately.

Supported lipid bilayers (SLB) were produced from a suspension of small unilamellar vesicles (SUVs), which were generated by hydration of a thin vacuum dried lipid film (same composition as for GUV production) using liposome buffer (12.5 mM Tris HCl pH 7.4, 137.5 mM NaCl, 0.1 mM DTT and 1 mM ATP/Mg^{2+}). The suspension was subjected to 3-5 freeze-thawing cycles followed by sonication for 30 min. The size of liposomes was measured by dynamic light scattering. 200 µl of SUV suspension was supplemented with 1 mM $CaCl_2$ and deposited either on freshly generated silanized mica or plasma cleaned glass coverslips and incubated at room temperature for 30 min. Unbound vesicles were removed by washing with SEC buffer.

Reconstitution of LC3B conjugation reaction

LC3B was preincubated with ATP/Mg^{2+}, DTT, ATG7 and ATG3 at 37°C for 30 min before reconstituted ATG12–ATG5-ATG16L1 (variant) complexes were added. 100 µL of the mixture was added to 100 µL of GUV suspension in IBIDI chambers to reach final concentrations of 1 mM ATP/Mg^{2+}, 0.1 mM DTT, 1 µM ATG7, 1.5 µM ATG3, 6 µM LC3B (2:1 ratio of unlabeled to labelled) and 1 µM ATG12-ATG5-ATG16L1, and incubated for 1 h at 37°C. The conjugation of LC3B to SLBs was carried out as described for GUVs using AFM chambers and unbound protein was removed by extensive washing with SEC buffer.

Confocal Microscopy

Confocal images of GUVs and fixed cells were acquired on a Leica TCS SP8 AOBS Confocal Laser Scanning Microscope (×63/1.4 NA objective) using the Leica LAS AF SP8 software. Atto405, GFP/$Alexa^{488}$, rhodamine/mCherry/RFP/$Alexa^{561}$, and $Alexa^{633}$ dyes were excited with 405 nm, 488 nm, 561 nm and 633 nm laser light, respectively. Multi-tracking was used for image acquisition and pinholes were set for acquisition of 0.5-1.0 µm optical slices. Images were analyzed using either ImageJ or Fiji.

Fluorescence Recovery after Photobleaching

FRAP experiments were performed using a Leica-TCS-SP8 microscope. The images were acquired using a 63x objective with a resolution of 512 x 512 pixel and a pinhole set to 1.0 µm. Fluorescence corresponding to 10 % of the total GUV area or of indicated SLB areas was bleached using 100 % laser power. Recovery was observed by recording 104 frames over 6-8 min. Images were analyzed using Fiji using a non-bleached part of the same GUV to correct for bleaching during recovery and background fluorescence. FRAP curves were fitted to the exponential decay function y = a (1 − e (−xb)) with mobile fractions = a and half-times t1/2 = −log (0.5)/b.

Atomic Force Microscopy

The atomic force microscopy was performed on a BRUKER ScanAsyst. Peak force tapping mode AFM images were acquired using SCANASYST-FLUID cantilevers (BRUKER). The peak force oscillation frequency was set to 150 kHZ and the set point was assigned to 200 pN. Resolution of images were 512 x 512 pixels.

Cloning

Plasmids and primers are listed in Table S2. The cDNA clones coding for ATG7 (isoform 1), ATG3, ATG12, ATG5, ATG16L1 and LC3B were cloned as described previously[19]. HA-tagged ATG16L1 was generated by cloning a 3x HA-tag and the cDNA of ATG16L1, separated by a linker (AQCS $(GA)_6$GPTENSS), into pLPCX (Clontech) between *Hind*III and *Not*I restriction sites. ATG16L1 truncations were amplified by PCR using the full-length construct as template and cloned into the pLPCX vector using the same restriction sites. RFP-GFP-LC3B was generated by inserting the cDNA of LC3B into pTfLC3 (Addgene plasmid #21074) using *Bgl*II and *Kpn*I restriction sites. Cloning of the GFP-LC3B construct and generation of CRISPR-Cas9 ATG16 knock out cells was described previously[19] and both mCherry-WIPI2b-CAAX and WIPI2b-CAAX constructs were a gift from Sharon Tooze[18]. ATG14 cDNA from pEGFP-ATG14L (Addgene plasmid # 21635) was inserted into pmKate2-C1 (Euromedex EV-FP181) using the compatible restriction sites EcoRI and KpnI. Site-directed mutagenesis was used to restore the reading frame by inserting an adenine at position 1331.

LC3B lipidation assay

ATG16L1 knock out HeLa cells were rescued by transfecting N-terminal HA tagged ATG16 variants or full-length ATG16L1 as indicated for 24 h. Cells were washed with PBS and starved for 2 h in EBSS. The cells were harvested following trypsination and lysed with lysis buffer (150 mM NaCl, 1 % NP-40, 50 mM Tris pH 7.4) supplemented with 1 mM PMSF (Roth) and complete protease inhibitor cocktail (Sigma Aldrich; Roche) for 30 min on ice. The cell lysate was centrifuged at 10000 g for 10 min. The protein concentration of the supernatant was measured by Pierce BCA protein assay kit (Thermo Fischer). Equal amounts of cell lysate mixed with 5x sample buffer was subjected to NUPAGE 4-12 % Bis-Tris Gel (Invitrogen), transferred to PVDF membrane and blotted with specific primary antibody and HRP-conjugated secondary antibodies. Membrane was thoroughly washed 3 times and developed with Super signal West Pico chemiluminescent substrate (Thermo Fischer). Detection was performed by a GelDoc documentation system and analysis by ImageJ.

Cytosol and membrane fraction (Cell fractionation)

Membrane fractions were prepared as previously reported[30]. Cells were harvested by centrifugation at 1500 g for 10 min and the pellet was dissolved in fractionation buffer (20 mM HEPES-KOH pH 7.4, 100 mM potassium acetate, 85 mM sucrose, 1 mM magnesium acetate supplemented with 1 mM PMSF and complete protease inhibitor cocktail). Cell lysis was performed by applying three freeze-thawing cycles and cell lysate was centrifuged at 1500 g for 5 min. The soluble cytoplasmic fraction was prepared by centrifugation of the supernatant at 70000 g for 30 min. The pellets from both the spins were dissolved in fractionation buffer containing 1 % NP-40 and centrifuged at 70000 g for 30 min. The supernatant from the second-high speed run corresponds to the membrane fraction and was together with the cytosolic fractions analyzed by western blotting.

Starvation-dependent recruitment of LC3B to the PM

Cells plated onto 24-well plate coverslips were transfected with 350 ng of mCherryWIPI2-CAAX and 200 ng of3HA-LC3B using Mirus Hela Monster kit (Mirus 2904) according to manufacturer's instructions. One day post-transfection, cells were washed with PBS and incubated with EBSS starvation medium for indicated times at 37°C in a 5% CO_2 atmosphere. Cells were fixed in 4% PFA for 10 minutes and permeabilized with ice-cold methanol for 5 minutes at RT. 3xHA-LC3B was stained using an anti-HA primary and an Alexa 488 secondary antibody and DAPI for nuclei. Cells were mounted on glass slides with Fluoromont G mounuting medium and randomly imaged at the confocal microscope. The number of LC3B puncta per each cell was first calculated using ComDet plugin and divided by the area of the corresponding cell in order to have the LC3B puncta per mm^2. The percentage of the LC3B puncta at the PM was obtained by dividing the LC3B puncta calculated using the ComDet plugin at the PM (1.5 µm width from the PM) to the total and multiplied by 100.

GFP-RFP-LC3B degradation assay

ATG16L1 KO cells were transduced with lentiviruses carring ATG16L1 variants under the control of a CMV promoter. Viruses were produced by transfecting HEK-293T cells with plvX-Puro-ATG16L1 variant plasmids, psPAX2 and pmd2G using the Jet prime transfection kit. Supernatant with viral particles was collected four days post transfection and applied to HeLa ATG16L1 KO cells for 48 hours. Transduced cells were selected by puromycin treatment (2µg/ml) and single clones were selected by plating diluted cell suspensions. ATG16L1 expression levels were analyzed by western blotting using an ATG16L1 selective antibody. Clones expressing ATG16L1 at native levels were transfected with RFP-GFP-LC3B plasmid (see cloning) and cells were starved as described above. Cells were imaged using a Leica SP8 confocal microscope with an 63x oil objective.

Autophagy inhibition

HeLa cells were plated onto 24-well plate coverslips and transfected with 350 ng of mCherry-WIPI2-CAAX, 200 ng of 3xHA-LC3B using the Mirus HeLa Monster kit, according to manufacturer's instructions. At 24 h post-transfection, cells were treated with 0.5 µM SAR405 (Ape Bio A8883) for 8 h (or DMSO, control) followed by starvation for 2 h in EBSS (or fed in full DMEM). Alternatively, cells were incubated with 10 µM SBI-0206965 (Sigma Aldrich, SML1540; or DMSO, control) and starved for 2 h in EBSS medium (or fed in full DMEM). Cells were fixed in 4% PFA for 10 minutes and permeabilized with ice-cold methanol for 5 minutes at RT. Immunostaining of 3xHA-LC3B, images acquisition and analysis were performed as in "Starvation-dependent recruitment of LC3B to the PM" section.

Quantification of LC3B and ATG16L1 puncta

Z-stacks were converted into maximum projections using Fiji and LC3B punctae were counted using the Particle Analysis Plugin. For each projection, a threshold was manually set to identify particles of interest. The particles were analysed using a size range from 0.2 to 1 µm and a circularity between 0 to 1. The number of punctae per cell was assessed in 10 randomly chosen fields of view per condition. The same procedure was used to count ATG16L1 punctae, but the size range was set to 0.1-0.7 µm and 0.7-2.0 µm, respectively.

siRNA treatment

Semiconfluent HeLa cells were transfected with control (scrambled), ATG14 or ULK1 siRNA. All siRNA treatments were performed in serum- and antibiotic-free culture medium, using JetPRIME ® (Polyplus 114-01) according to manufacturer's instructions. After 24 h, the medium was replaced by fresh full DMEM and DNA transfection (350 ng of mCherry-WIPI2-CAAX and 250 ng of3xHA-LC3B) was carried out using *Trans*IT-HeLa MONSTER (Mirus 2904) and incubated 24 h. Cells were washed with PBS, fixed in 4% PFA, permeabilized in ice-cold methanol for 5 minutes at RT, immunostained for HA and analysed by immunofluorescence and western blot.

3D STORM

3D STORM (Stochastic Optical Reconstruction Microscopy) experiments were performed by placing fixed and stained cells on coverslips in a switching buffer prepare freshly before imaging (Tris 50 mM, NaCl 10 mM, 10% glucose, Glucose oxidase 0.5 mg/mL, Catalase 50 µg/mL, MEA 100mM pH8.3).
The super-resolved images were acquired on an Elyra 7 3D SMLM microscope (Carl Zeiss, Germany) using a 63X/1.4 oil objective with a 1.518 refractive index oil (Carl Zeiss) and an sCMOS PCO Edge 4.2 camera for the detection. 3D STORM was performed using 'double phase ramp' optical component and calibrated with fluorescent beads. All processing was performed with the Zen software. The localization of individual molecules was determined using a peak mask size of 15 pixel and a peak intensity to noise of 5. Drift correction was corrected using model-based algorithm. Final images were generated with a resolution of 50 nm in Z and 10 nm X in Y.

Cell unroofing and immunogold labeling

Unroofing was performed by sonication as previously described [52]. Coverslips where quickly rinsed three times in Ringer+Ca (155 mM NaCl, 3 mM KCl, 3 mM NaH_2PO_4, 5 mM HEPES, 10 mM glucose, 2 mM $CaCl_2$, 1 mM $MgCl_2$, pH 7.2), then immersed 10 s in Ringer-Ca (155 mM NaCl, 3 mM KCl, 3 mM NaH_2PO_4, 5 mM HEPES, 10 mM glucose, 3 mM EGTA, 5 mM $MgCl_2$, pH 7.2) containing 0.5 mg/mL poly-L-lysine) and quickly rinsed in Ringer-Ca. Cells were unroofed by scanning the coverslip with rapid (2-5 s) sonicator pulses at the lowest deliverable power in KHMgE buffer (70 mM KCl, 30 mM HEPES, 5 mM $MgCl_2$, 3 mM EGTA, pH 7.2).
Unroofed cells were immediately fixed using fixative in KHMgE: 4 % PFA for 45 min for PREM of immunogold-labeled samples, 3 % PFA and 1 % glutaraldehyde or 2 % PFA and 2 % glutaraldehyde for 10 to 20 min for PREM. Glutaraldehyde-fixed samples were subsequently quenched using 0.1% $NaBH_4$ in KHMgE for 10 minutes. Immunogold labeling was performed in detergent-free buffer (KHMgE, 1 % BSA), samples were blocked for 30 min, incubated 1 h and 30 min with the primary antibody (using a 1:20 dilution), rinsed and incubated two times 20 min with the gold-coupled secondary antibodies. Samples were rinsed again and post-fixed with 2% glutaraldehyde.

Platinum-replica sample processing

Cells and SLBs were further sequentially treated with 0.5 % OsO_4, 1 % tannic acid and 1 % uranyl acetate prior to graded ethanol dehydration and hexamethyldisilazane substitution (HMDS, Sigma). Dried samples were then rotary-shadowed with 2 nm of platinum and 5-8 nm of carbon using an ACE600 high vacuum metal coater (Leica Microsystems). The resultant platinum replicas were floated off the glass with hydrofluoric acid (5 %), washed several times on distilled water, and picked up on 200 mesh formvar/carbon-coated EM grids.

EM of platinum replicas

Replicas on EM grids were mounted in a eucentric side-entry goniometer stage of a transmission electron microscope operated at 80 kV (model CM120; Philips) and images were recorded with a Morada digital camera (Olympus). Images were processed in Photoshop (Adobe) to adjust brightness and contrast and presented in inverted contrast. Tomograms were made by collecting images at the tilt angles up to ± 25° relative to the plane of the sample with 5° increments. Images were aligned by layering them on top of each other in Photoshop. Measurements of cup length and width were performed on high magnification PREM views using ImageJ.

Quantification of membrane structures in platinum replicas

For in vitro experiments, we distinguished three morphologies based on analyzing line profiles using image J. Rims: circular structures with a line profile with two distinct maxima over background with a grey value > 3-times over background and a length of < 25 nm. Premature cups: asymmetric circular structures with a line profile with two distinct maxima with a grey value > 3-times over background, dimensions of one miximum < 25 nm and that of the other maximum < ½ of diameter of the structure. Expanded cups: asymmetric circular structures with a line profile with two distinct maxima with a grey value > 3-times over background, dimensions of one miximum < 25 nm and that of the other maximum > ½ of diameter of the structure.
For in vivo experiments, we distinguished four morphologies. Rims, premature cups and expanded cups were defined as for in vitro experiments. Line profiles of autophagic vesicles did not show two distinct maxima but one extended plateau with dimensions between 200 and 600 nm. Structures that did not fit the criteria were not considered.

Correlative light platinum replica EM

For correlative light PREM, ATG16L1 knockout HeLa cells expressing Wipi2bCAAX, HA-ATG16L1, and LC3B were grown on alpha-numerically gridded bottom chambers (Ibidi, France) for 48 hours. Unroofing of cells was prepared as described above and adherent plasma membranes were immediately immersed in 4% paraformaldehyde for 30 minutes at room temperature. After rinses, the plasma membrane was blocked for 1 hour at room temperature in saturation buffer (1% BSA in KHMgE buffer). After HA-ATG16L1 and LC3B were labeled with corresponding HA (Mouse) and LC3B (Rabbit) primary antibodies [52] for 2 hours at room temperature. After washing three times,

adherent membranes were incubated in Alexa fluor 488 anti-rabbit (Invitrogen, A11034) and Alex fluor 647 anti-mouse (Invitrogen, A31571) secondary antibodies diluted in KHMgE buffer for 1 hour. Fluorescence images were acquired with a Nikon Ti2 microscope at a magnification of 100X objective lenses, and super-resolution images were obtained with the LiveSR module (Gataca Systems). After the acquisition of fluorescence images, the samples were then incubated in 2% glutaraldehyde and 2% paraformaldehyde at 4°C overnight and processed as described previously to get the platinum replicas. Super-resolution microscopy and electron microscopy images were overlaid using Adobe Photoshop software to adjust brightness and contrast, and unroofed PMs are presented in inverted contrast.

Transmission Electron Microscopy

Cells were fixed with 4 % paraformaldehyde and 0.2 % glutaraldehyde for 10 min followed by 2 % paraformaldehyde and 0.1 % glutaraldehyde for two hours at RT. Cells were washed with PBS and 1% gelatin in PBS was added before cells were collected, pelleted (5000 g, 5 min) and resuspended in 10% gelatin (5 min at 37°C). Cells were again collected (8000 g, 5 min), the pellet was cut into blocks and incubated in 2.3 M sucrose solution at 4°C overnight. Blocks were frozen in liquid nitrogen and 150 nm ultrathin sections were prepared using a Leica-UC6-FC6 ultramicrotome equipped with a Leica 16DIA.DCIMM3530 diamond knife at -120 °C with a speed of 0.8 mm/s. Ribbons were mounted on carbon-coated copper finder grids (Oxford instruments, #AGG245) and tomograms were recorded using a Tecnai Biotwin 120 electron microscope at magnification of 23,000x with a tilt range from 50° to -50° and 5° increments. Tilt series were aligned and reconstructed using the IMOD software package and further processed with Amira 2019.3 (Thermo Fisher Scientific).

Correlative Large Volume Focused Ion Beam Scanning Electron Microscopy

ATG16L1 KO cells expressing mCherry-ATG16L1 variants were cultured in MatTek dishes with finder grid. Cells were washed three times with 1X PHEM buffer (5 min each) and postfixed with 1% osmium (EMS) and 1.5% potassium ferrocyanide (Sigma-Aldrich) in 1X PHEM buffer for 1 h. Samples were treated for 30 min with 1% tannic acid (Sigma-Aldrich) and 1 h with 1% osmium tetroxide (EMS), rinsed in water, and incubated in 1% uranyl acetate dissolved in 25% ethanol for 30 min. Cells were dehydrated in an ethanol (Sigma-Aldrich) series of 25%, 50%, 75%, 95% (5 min each), and three times in 100% (10 min each). Cells were embedded in epoxy resin (EMS) after 48 h at 60°C of polymerization. Embedded samples were mounted on aluminum stubs. Tomographic datasets were obtained using a field emission scanning electron microscope (FESEM) Zeiss Auriga microscope equipped with a CrossBeam workstation (ZEISS) and acquired using ATLAS 3D software (ZEISS). The specimen stage was tilted at 54° with 5 mm working distance of the pole piece, at the coincidence point of the electron and the galion beams. The milling conditions for the trench that allowed the view of the cross-section were 20 nA at accelerating voltage of 30 kV. The fine polishing of the surface block was performed with 10 nA at 30 kV. For the slice series, the conditions were as follows: 0.5 nA milling current of the Gallium emitter leading to the removal of 10 nm at a time from the epoxy resin. Scanning EM images were recorded with an aperture of 60 µm in the high-current mode at 2 kV of the in-lens EsB detector with the EsB grid set to −1,000 V. Voxel size was 10 nm in x/y and 10 nm in z. Contrast of the images was inverted to conventional brightfield.

Data processing and 3D reconstruction

Alignment of image stacks was done with the open source software ImageJ for data alignment (National Institutes of Health; Schneider et al., 2012) and Amira Software for visualization (Amira 3D 2022.1 ; ThermoFisher Scientific). Segmentation and 3D reconstructions were performed semiautomatically using Amira software and were corrected manually.

Serial sectionning transmission electron microscopy

Cells were washed three times with 1X PHEM buffer (5 min each) and postfixed with 1% osmium (EMS) and 1.5% potassium ferrocyanide (Sigma-Aldrich) in 1X PHEM buffer for 1 h. Samples were treated for 30 min with 1% tannic acid (Sigma-Aldrich) and 1 h with 1% osmium tetroxide (EMS), rinsed in water, and incubated in 1% uranyl acetate dissolved in 25% ethanol for 30 min. Cells were dehydrated in an ethanol (Sigma-Aldrich) series of 25%, 50%, 75%,

95% (5 min each), and three times in 100% (10 min each). Cells were embedded in epoxy resin (EMS) after 48 h at 60°C of polymerization. For the correlative microscopy, the region of interest was determined thanks to landmarks printed below embedded samples. Embedded cells were sectioned with an ultramicrotome (Leica, UC7) with 70 nm thickness. Thin serial sections were collected on a single slot grid (Agar scientific). Serial sections were observed with a transmission electron microscope TEM Tecnai T12 (ThermoFisher) at 120kV and imaged using a US4000 camera (Gatan).

QUANTIFICATION AND STATISTICAL ANALYSIS

Quantifications were performed from at least three (two for cell fractionation) independent experiments or from at least 20 cells and values are expressed as mean ± standard deviation. All parameters including significance and n-values are specified in each Fig. legend. Statistical significance between two independent samples was determined using a two tailed unpaired t-test. P values of < 0.05 were considered statistically significant and significance levels were indicated by *P< 0.05; **P< 0.01; ***P< 0.001. The corresponding charts were generated by GraphPad Prism.

DATA AND SOFTWARE AVAILABILITY

Source data are provided in Table **S1**

References

1. Galluzzi, L. *et al.* Molecular definitions of autophagy and related processes. *Embo J* **36**, 1811–1836 (2017).

2. Kirkin, V. & Rogov, V. V. A Diversity of Selective Autophagy Receptors Determines the Specificity of the Autophagy Pathway. *Mol Cell* **76**, 268–285 (2019).

3. González, A. & Hall, M. N. Nutrient sensing and TOR signaling in yeast and mammals. *Embo J* **36**, 397–408 (2017).

4. Johansen, T. & Lamark, T. Selective Autophagy: ATG8 Family Proteins, LIR Motifs and Cargo Receptors. *J Mol Biol* **432**, 80–103 (2019).

5. Eickhorst, C., Licheva, M. & Kraft, C. Scaffold proteins in bulk and selective autophagy. *Prog Mol Biol Transl* **172**, 15–35 (2020).

6. Orsi, A. *et al.* Dynamic and transient interactions of Atg9 with autophagosomes, but not membrane integration, are required for autophagy. *Mol Biol Cell* **23**, 1860–1873 (2012).

7. Tito, S. D., Hervás, J. H., Vliet, A. R. van & Tooze, S. A. The Golgi as an Assembly Line to the Autophagosome. *Trends Biochem Sci* **45**, 484–496 (2020).

8. Ge, L., Melville, D., Zhang, M. & Schekman, R. The ER-Golgi intermediate compartment is a key membrane source for the LC3 lipidation step of autophagosome biogenesis. *eLife* **2013**, e00947 (2013).

9. Ravikumar, B., Moreau, K., Jahreiss, L., Puri, C. & Rubinsztein, D. C. Plasma membrane contributes to the formation of pre-autophagosomal structures. *Nat Cell Biol* **12**, 747–757 (2010).

10. Hailey, D. W. *et al.* Mitochondria Supply Membranes for Autophagosome Biogenesis during Starvation. *Cell* **141**, 656–667 (2010).

11. Dupont, N. *et al.* Neutral Lipid Stores and Lipase PNPLA5 Contribute to Autophagosome Biogenesis. *Curr Biol* **24**, 609–620 (2014).

12. Maeda, S., Otomo, C. & Otomo, T. The autophagic membrane tether ATG2A transfers lipids between membranes. *Elife* **8**, e45777 (2019).

13. Mizushima, N. The ATG conjugation systems in autophagy. *Curr Opin Cell Biol* **63**, 1–10 (2020).

14. Tanida, I., Tanida-Miyake, E., Komatsu, M., Ueno, T. & Kominami, E. Human Apg3p/Aut1p Homologue Is an Authentic E2 Enzyme for Multiple Substrates, GATE-16, GABARAP, and MAP-LC3, and Facilitates the Conjugation of hApg12p to hApg5p*. *J Biol Chem* **277**, 13739–13744 (2002).

15. Sou, Y. *et al.* The Atg8 Conjugation System Is Indispensable for Proper Development of Autophagic Isolation Membranes in Mice. *Mol Biol Cell* **19**, 4762–4775 (2008).

16. Tanida, I. *et al.* HsAtg4B/HsApg4B/Autophagin-1 Cleaves the Carboxyl Termini of Three Human Atg8 Homologues and Delipidates Microtubule-associated Protein Light Chain 3- and GABAA Receptor-associated Protein-Phospholipid Conjugates*. *J Biol Chem* **279**, 36268–36276 (2004).

17. Fujita, N. *et al.* The Atg16L complex specifies the site of LC3 lipidation for membrane biogenesis in autophagy. *Mol Biol Cell* **19**, 2092 2100 (2008).

18. Dooley, H. C. *et al.* WIPI2 Links LC3 Conjugation with PI3P, Autophagosome Formation, and Pathogen Clearance by Recruiting Atg12–5-16L1. *Mol Cell* **55**, 238–252 (2014).

19. Wetzel, L. *et al.* TECPR1 promotes aggrephagy by direct recruitment of LC3C autophagosomes to lysosomes. *Nat Commun* **11**, 2993 (2020).

20. Chen, D. *et al.* A Mammalian Autophagosome Maturation Mechanism Mediated by TECPR1 and the Atg12-Atg5 Conjugate. *Mol Cell* **45**, 629–641 (2012).

21. Nguyen, T. N. *et al.* Atg8 family LC3/GABARAP proteins are crucial for autophagosome–lysosome fusion but not autophagosome formation during PINK1/Parkin mitophagy and starvation. *J Cell Biol* **215**, 857–874 (2016).

22. Nguyen, T. N. *et al.* ATG4 family proteins drive phagophore growth independently of the LC3/GABARAP lipidation system. *Mol Cell* **81**, 2013-2030.e9 (2021).

23. Vaites, L. P., Paulo, J. A., Huttlin, E. L. & Harper, J. W. Systematic analysis of human cells lacking ATG8 proteins uncovers roles for GABARAPs and the CCZ1/MON1 regulator C18orf8/RMC1 in macro and selective autophagic flux. *Mol Cell Biol* **38**, e00392-17 (2017).

24. Tsuboyama, K. *et al.* The ATG conjugation systems are important for degradation of the inner autophagosomal membrane. *Science* **354**, 1036–1041 (2016).

25. Kabeya, Y. *et al.* LC3, a mammalian homologue of yeast Apg8p, is localized in autophagosome membranes after processing. *Embo J* **19**, 5720–5728 (2000).

26. Kaufmann, A., Beier, V., Franquelim, H. G. & Wollert, T. Molecular Mechanism of Autophagic Membrane-Scaffold Assembly and Disassembly. *Cell* **156**, 469–481 (2014).

27. Maruyama, T. *et al.* Membrane perturbation by lipidated Atg8 underlies autophagosome biogenesis. *Nat Struct Mol Biol* **28**, 583–593 (2021).

28. Otomo, C., Metlagel, Z., Takaesu, G. & Otomo, T. Structure of the human ATG12~ATG5 conjugate required for LC3 lipidation in autophagy. *Nat Struct Mol Biol* **20**, 59–66 (2013).

29. Fletcher, K. *et al.* The WD40 domain of ATG16L1 is required for its non-canonical role in lipidation of LC3 at single membranes. *Embo J* **37**, (2018).

30. Lystad, A. H. *et al.* Distinct functions of ATG16L1 isoforms in membrane binding and LC3B lipidation in autophagy-related processes. *Nat Cell Biol* **117**, 2805 (2019).

31. Dudley, L. J. *et al.* Intrinsic lipid binding activity of ATG16L1 supports efficient membrane anchoring and autophagy. *Embo J* **38**, e100554 (2019).

32. Archna, A. & Scrima, A. Identification, biochemical characterization and crystallization of the central region of human ATG16L1. *Acta Crystallogr Sect F Struct Biology Commun* **73**, 560–567 (2017).

33. Nascimbeni, A. C. *et al.* ER–plasma membrane contact sites contribute to autophagosome biogenesis by regulation of local PI3P synthesis. *Embo J* **36**, 2018–2033 (2017).

34. Kumar, S. *et al.* Mammalian hybrid pre-autophagosomal structure HyPAS generates autophagosomes. *Cell* (2021) doi:10.1016/j.cell.2021.10.017.

35. Kimura, S., Noda, T. & Yoshimori, T. Dissection of the Autophagosome Maturation Process by a Novel Reporter Protein, Tandem Fluorescent-Tagged LC3. *Autophagy* **3**, 452–460 (2007).

36. Mizushima, N. *et al.* Dissection of Autophagosome Formation Using Apg5-Deficient Mouse Embryonic Stem Cells. *J Cell Biology* **152**, 657–668 (2001).

37. Mizushima, N. *et al.* Mouse Apg16L, a novel WD-repeat protein, targets to the autophagic isolation membrane with the Apg12-Apg5 conjugate. *J Cell Sci* **116**, 1679–1688 (2003).

38. Kishi-Itakura, C., Koyama-Honda, I., Itakura, E. & Mizushima, N. Ultrastructural analysis of autophagosome organization using mammalian autophagy-deficient cells. *J Cell Sci* **127**, 4089–4102 (2014).

39. Uemura, T. *et al.* A Cluster of Thin Tubular Structures Mediates Transformation of the Endoplasmic Reticulum to Autophagic Isolation Membrane. *Mol Cell Biol* **34**, 1695–1706 (2014).

40. Jensen, L. E. *et al.* Membrane curvature sensing and stabilization by the autophagic LC3 lipidation machinery. *Science Adv.* **8**, eadd1436 (2022).

41. Zhang, W. *et al.* Autophagosome membrane expansion is mediated by the N-terminus and cis-membrane association of human ATG8s. *eLife* **12**, (2023).

42. Nath, S. *et al.* Lipidation of the LC3/GABARAP family of autophagy proteins relies on a membrane-curvature-sensing domain in Atg3. *Nat Cell Biol* **16**, 415 424 (2014).

43. Melia, T. J., Lystad, A. H. & Simonsen, A. Autophagosome biogenesis: From membrane growth to closure. *J Cell Biology* **219**, e202002085 (2020).

44. Hayashi-Nishino, M. *et al.* A subdomain of the endoplasmic reticulum forms a cradle for autophagosome formation. *Nat Cell Biol* **11**, 1433–1437 (2009).

45. Ylä-Anttila, P., Vihinen, H., Jokitalo, E. & Eskelinen, E.-L. 3D tomography reveals connections between the phagophore and endoplasmic reticulum. *Autophagy* **5**, 1180 1185 (2009).

46. Olivas, T. J. *et al.* ATG9 vesicles comprise the seed membrane of mammalian autophagosomes. *J Cell Biol* **222**, e202208088 (2023).

47. Osawa, T. *et al.* Atg2 mediates direct lipid transfer between membranes for autophagosome formation. *Nat Struct Mol Biol* **26**, 281–288 (2019).

48. Valverde, D. P. *et al.* ATG2 transports lipids to promote autophagosome biogenesis. *J Cell Biol* **218**, 1787–1798 (2019).

49. Matoba, K. *et al.* Atg9 is a lipid scramblase that mediates autophagosomal membrane expansion. *Nat Struct Mol Biol* **27**, 1185–1193 (2020).

50. Vliet, A. R. van *et al.* ATG9A and ATG2A form a heteromeric complex essential for autophagosome formation. *Mol Cell* (2022) doi:10.1016/j.molcel.2022.10.017.

51. Angelova, M. I. & Dimitrov, D. S. Liposome electroformation. *Faraday Discuss Chem Soc* **81**, 303–311 (1986).

52. Vassilopoulos, S., Gibaud, S., Jimenez, A., Caillol, G. & Leterrier, C. Ultrastructure of the axonal periodic scaffold reveals a braid-like organization of actin rings. *Nat Commun* **10**, 5803 (2019).

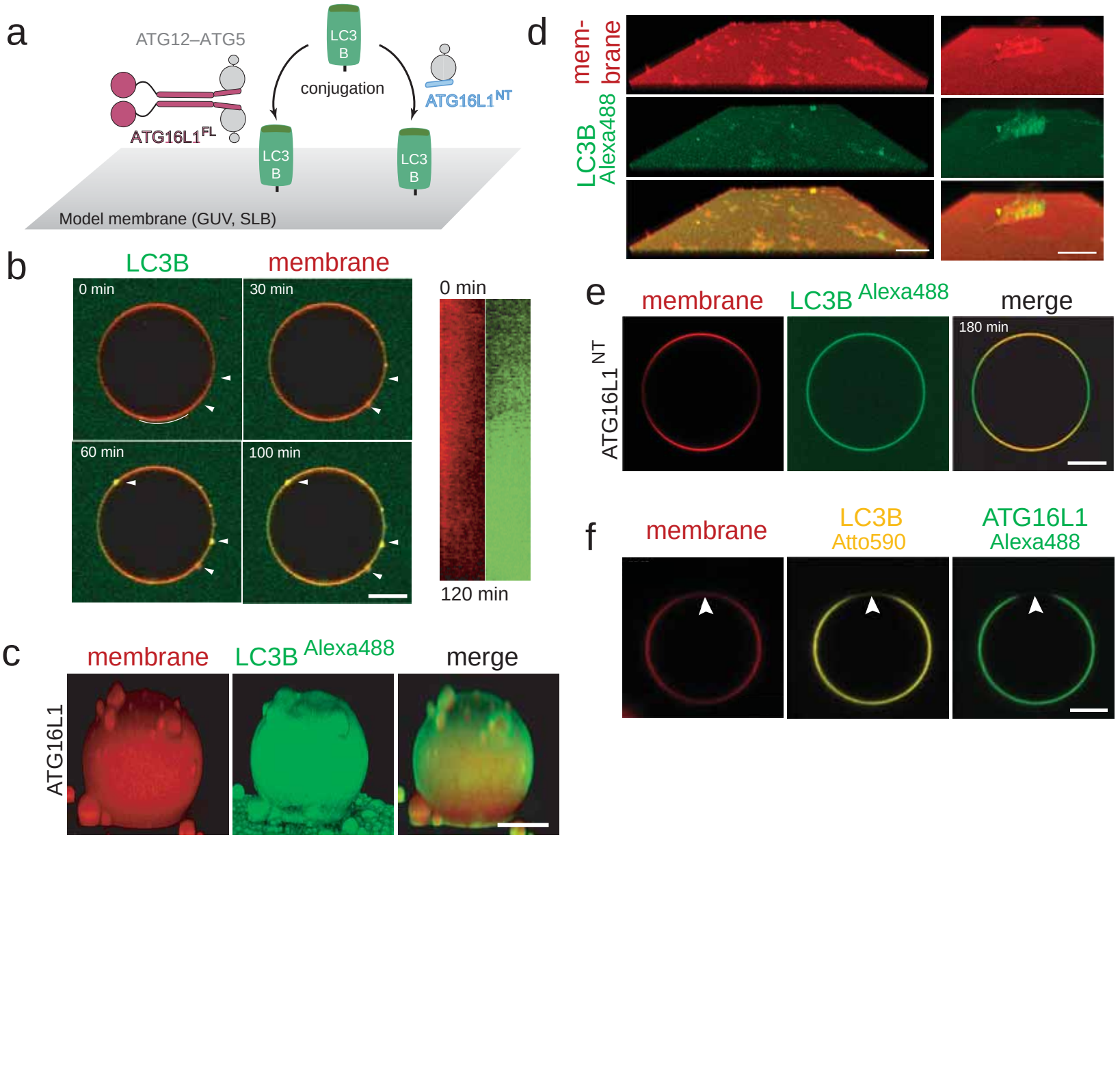
a
ATG12–ATG5
LC3 B
conjugation
ATG16L1NT
ATG16L1FL
LC3 B
LC3 B
Model membrane (GUV, SLB)
b
LC3B
membrane
0 min
30 min
60 min
100 min
0 min
120 min
c
membrane
LC3B Alexa488
merge
ATG16L1
d
mem-brane
LC3B Alexa488
e
membrane
LC3B Alexa488
merge
ATG16L1NT
180 min
f
membrane
LC3B Atto590
ATG16L1 Alexa488

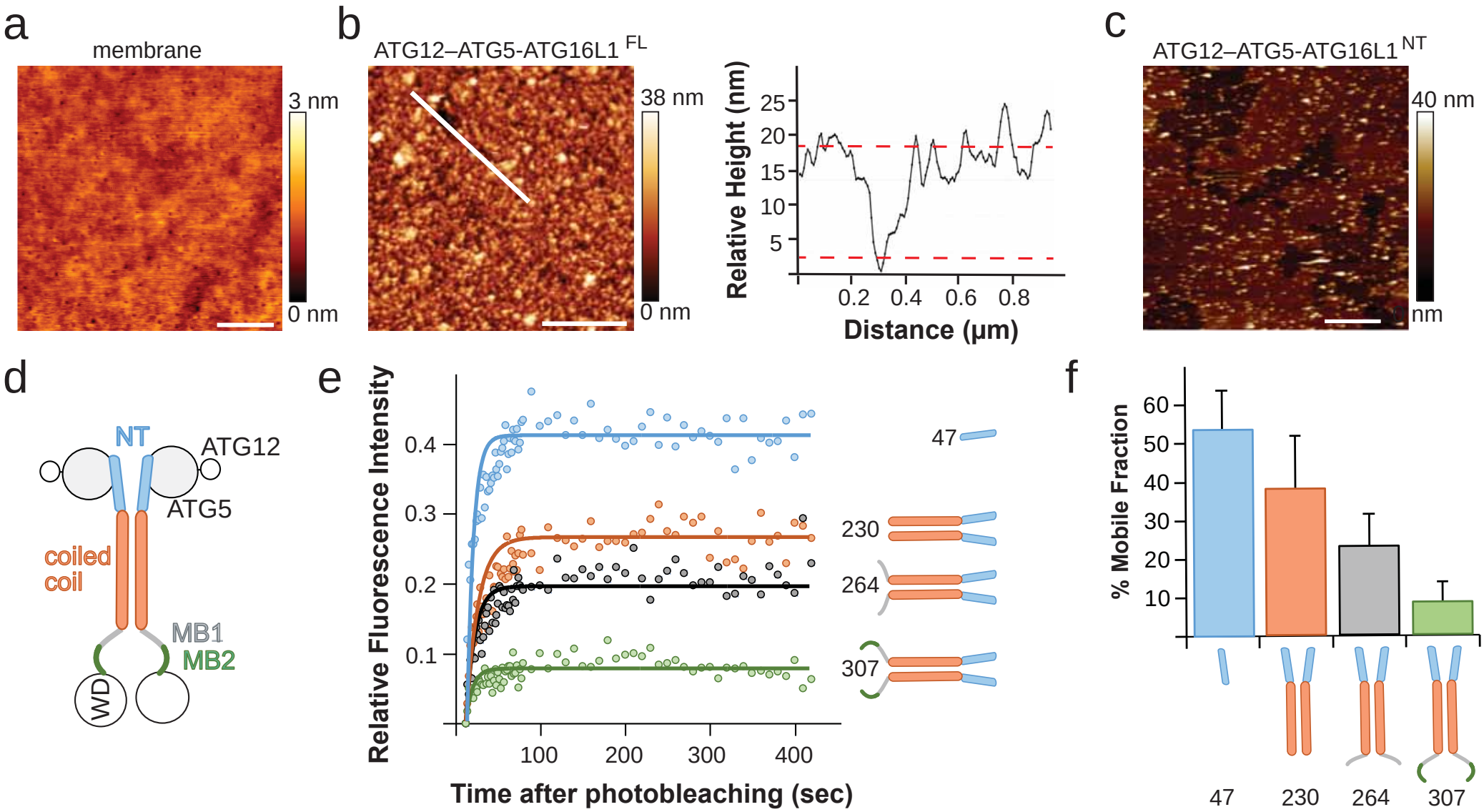
a
membrane
3 nm
0 nm
b
ATG12–ATG5-ATG16L1 FL
38 nm
0 nm
Relative Height (nm)
25
20
15
10
5
0.2
0.4
0.6
0.8
Distance (μm)
c
ATG12–ATG5-ATG16L1 NT
40 nm
0 nm
d
NT
ATG12
ATG5
coiled coil
MB1
MB2
WD
e
Relative Fluorescence Intensity
0.4
0.3
0.2
0.1
100
200
300
400
Time after photobleaching (sec)
47
230
264
307
f
% Mobile Fraction
60
50
40
30
20
10
47
230
264
307

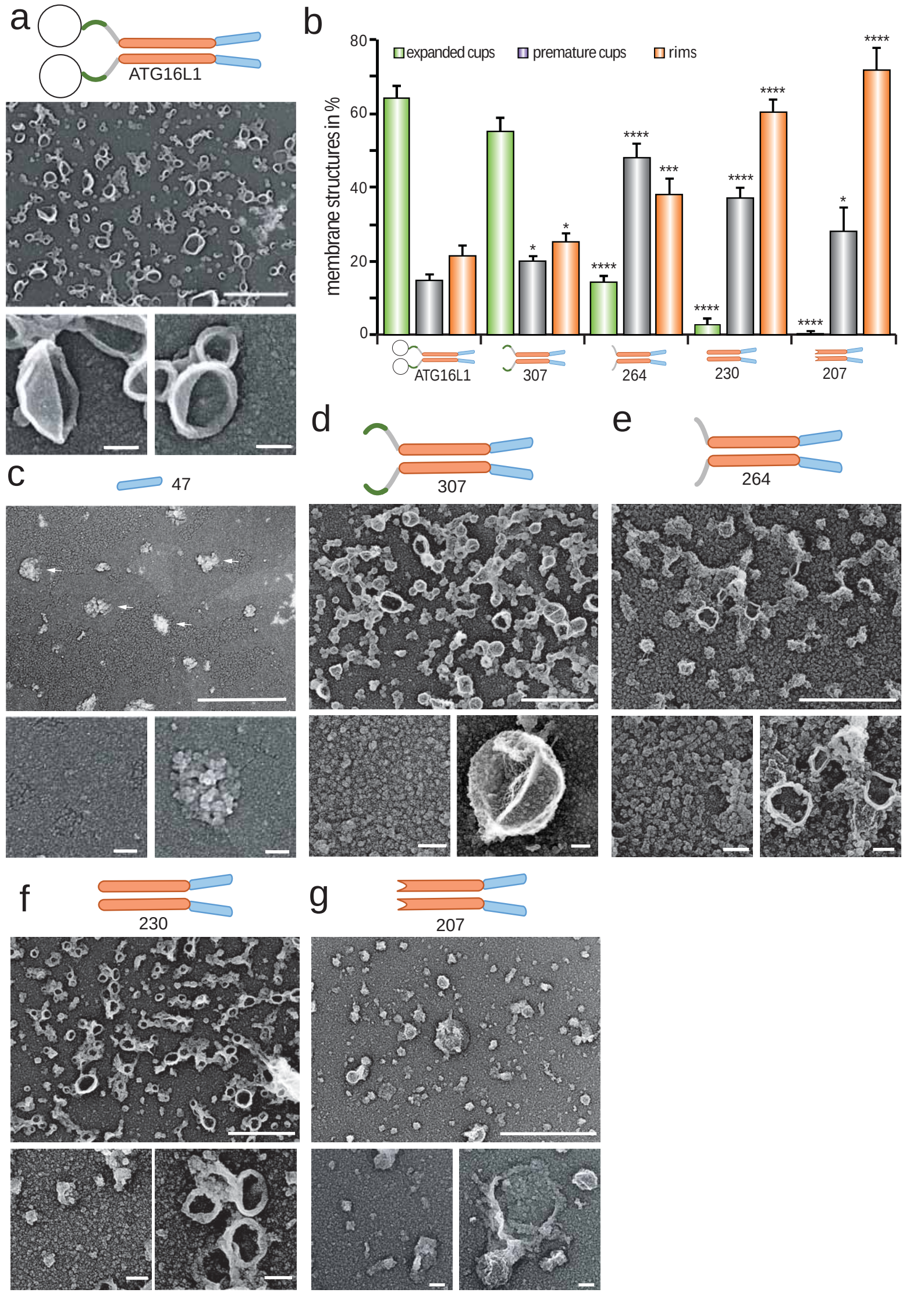
a
ATG16L1
b
membrane structures in %
expanded cups
premature cups
rims
ATG16L1
307
264
230
207
c
47
d
307
e
264
f
230
g
207

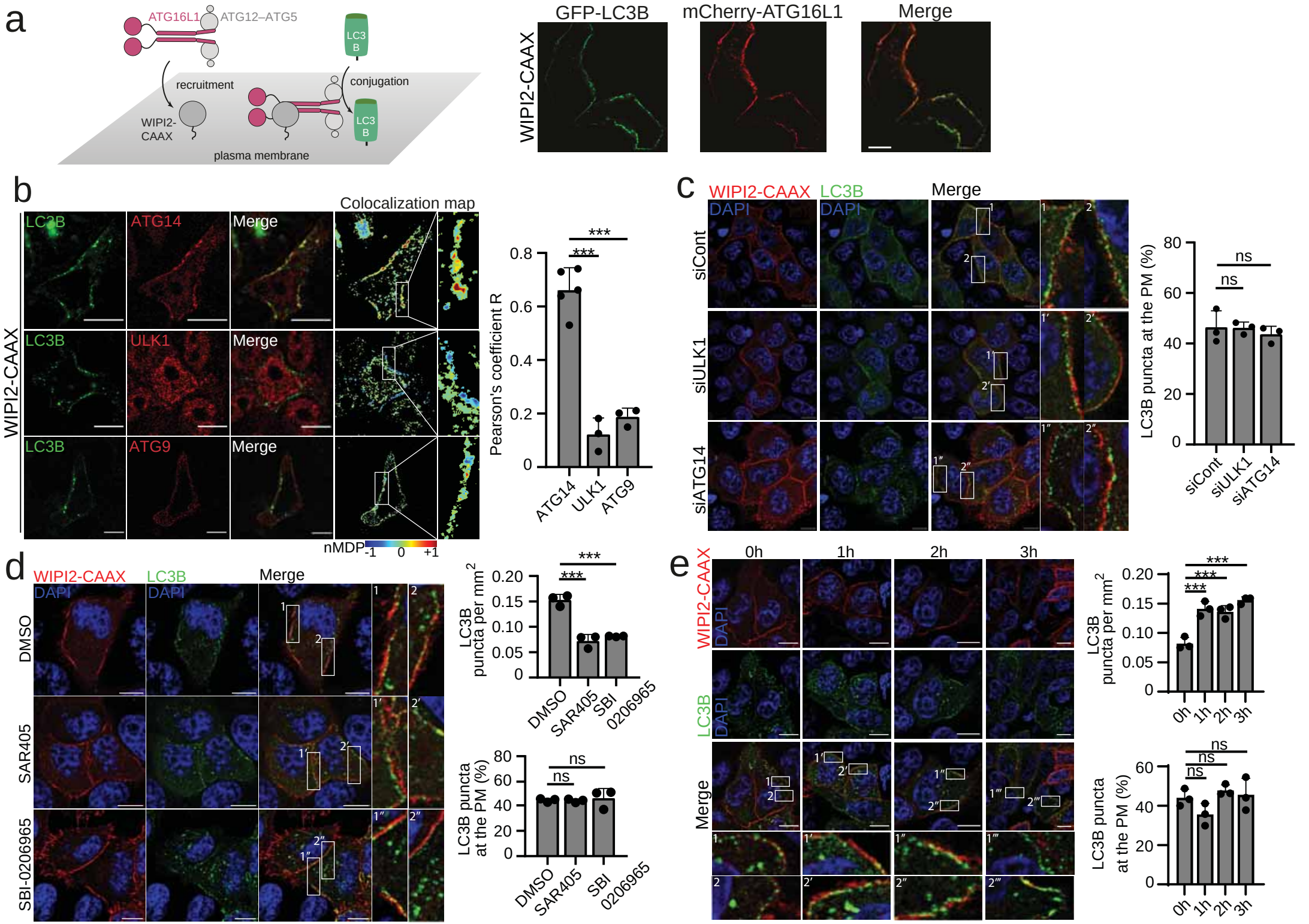
a
ATG16L1
ATG12–ATG5
LC3 B
recruitment
conjugation
WIPI2-CAAX
LC3 B
plasma membrane
GFP-LC3B
mCherry-ATG16L1
Merge
WIPI2-CAAX
b
Colocalization map
LC3B
ATG14
Merge
LC3B
ULK1
Merge
LC3B
ATG9
Merge
WIPI2-CAAX
nMDP -1 0 +1
Pearson's coefficient R
0.8
0.6
0.4
0.2
0
***
***
ATG14
ULK1
ATG9
c
WIPI2-CAAX
LC3B
Merge
DAPI
DAPI
siCont
siULK1
siATG14
LC3B puncta at the PM (%)
80
60
40
20
0
ns
ns
siCont
siULK1
siATG14
d
WIPI2-CAAX
LC3B
Merge
DAPI
DAPI
DMSO
SAR405
SBI-0206965
LC3B puncta per mm2
0.20
0.15
0.10
0.05
0
***
***
DMSO
SAR405
SBI 0206965
LC3B puncta at the PM (%)
80
60
40
20
0
ns
ns
DMSO
SAR405
SBI 0206965
e
0h
1h
2h
3h
WIPI2-CAAX
DAPI
LC3B
DAPI
Merge
LC3B puncta per mm2
0.20
0.15
0.10
0.05
0
***
***
***
0h
1h
2h
3h
LC3B puncta at the PM (%)
60
40
20
0
ns
ns
ns
0h
1h
2h
3h

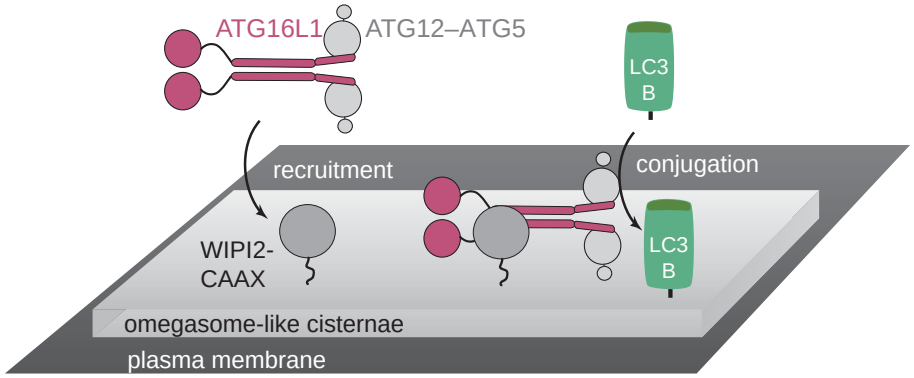
ATG16L1
ATG12–ATG5
LC3
B
recruitment
conjugation
WIPI2-
CAAX
LC3
B
omegasome-like cisternae
plasma membrane

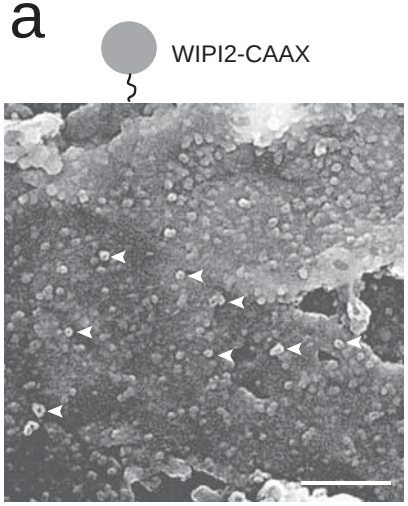
a
WIPI2-CAAX

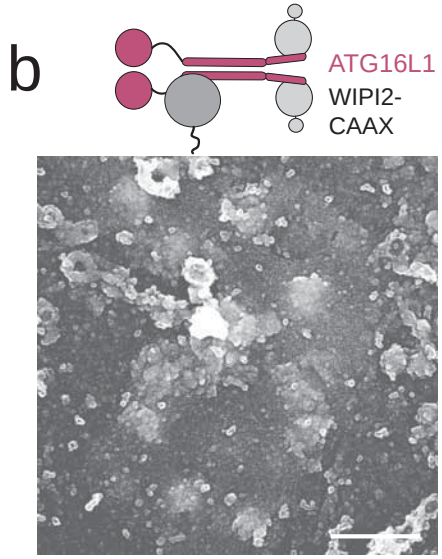
b
ATG16L1
WIPI2-
CAAX

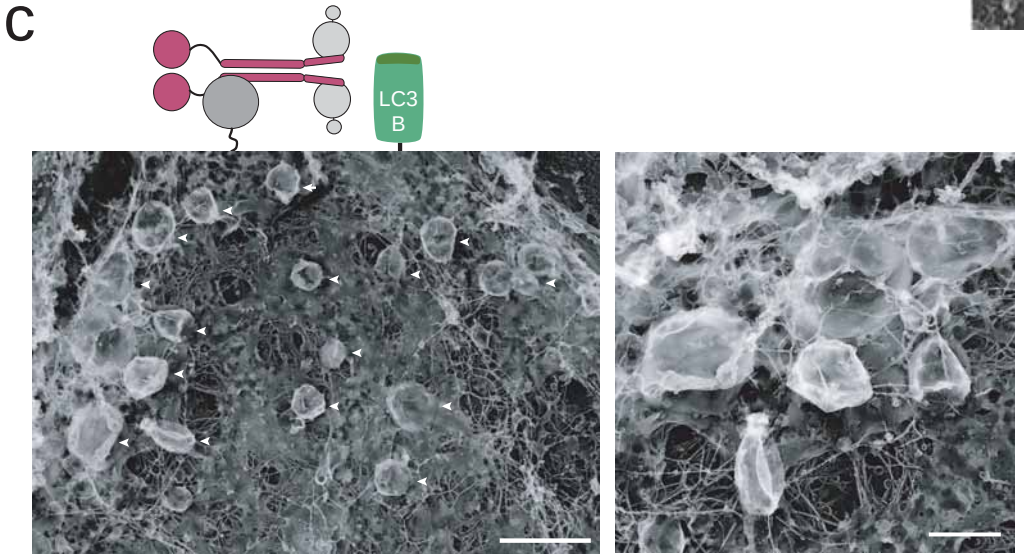
c
LC3
B

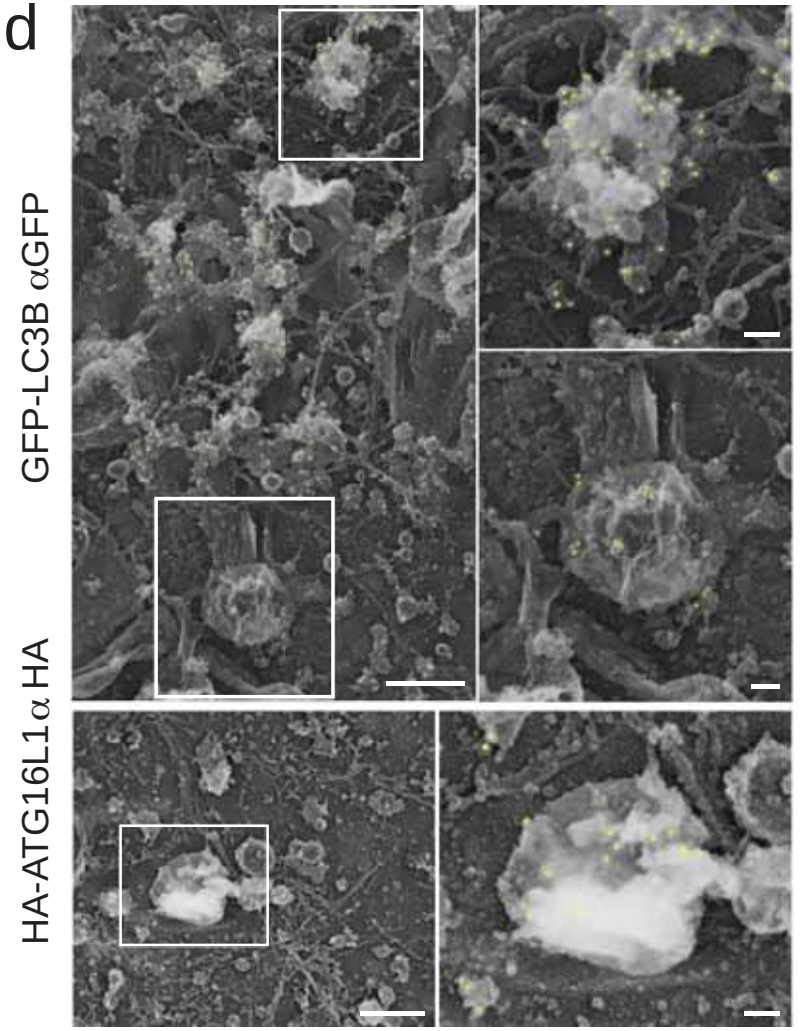
d
GFP-LC3B αGFP
HA-ATG16L1α HA

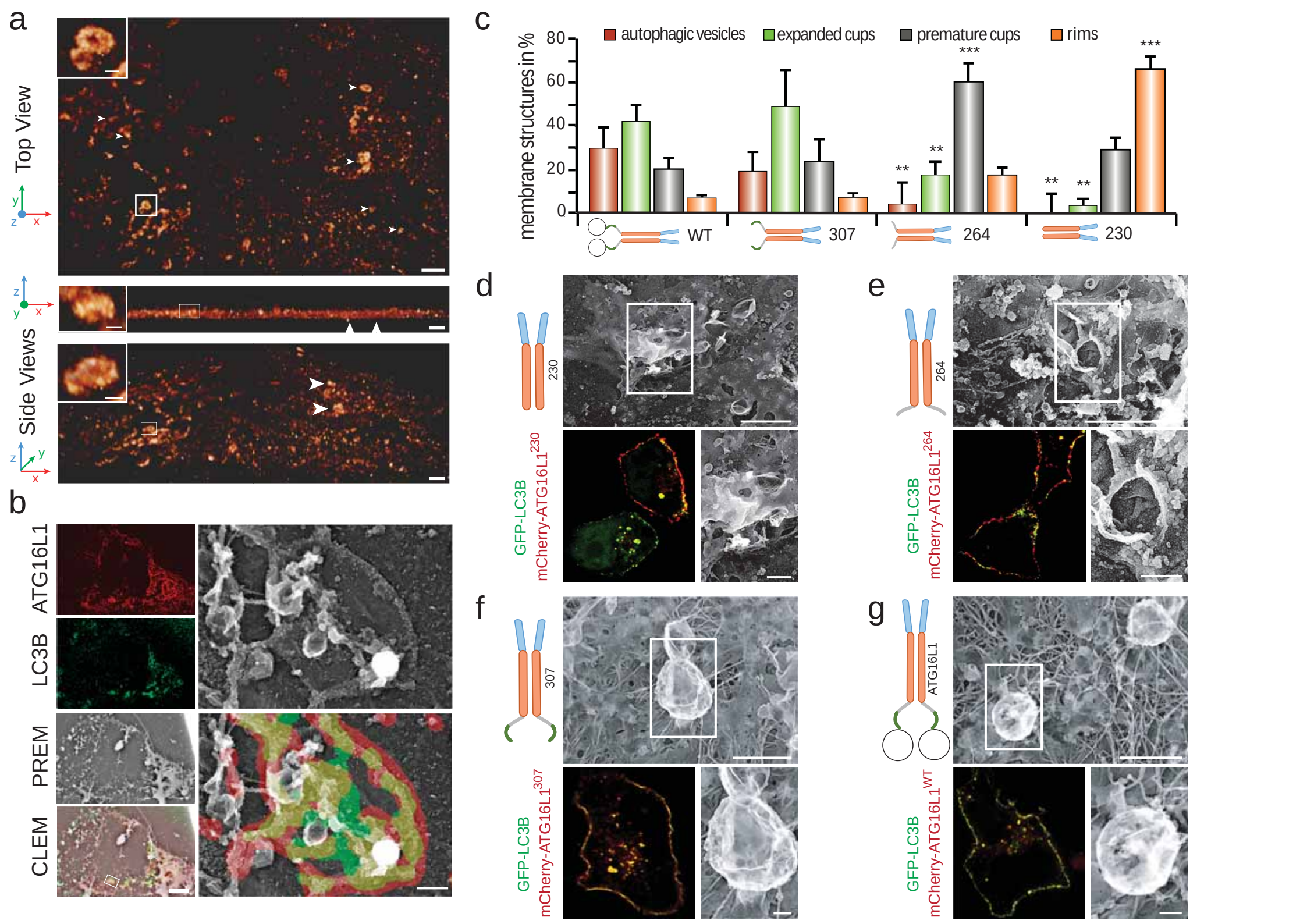
a
Top View
Side Views
b
ATG16L1
LC3B
PREM
CLEM
c
membrane structures in %
autophagic vesicles
expanded cups
premature cups
rims
WT
307
264
230
d
230
GFP-LC3B
mCherry-ATG16L1230
e
264
GFP-LC3B
mCherry-ATG16L1264
f
307
GFP-LC3B
mCherry-ATG16L1307
g
ATG16L1
GFP-LC3B
mCherry-ATG16L1WT

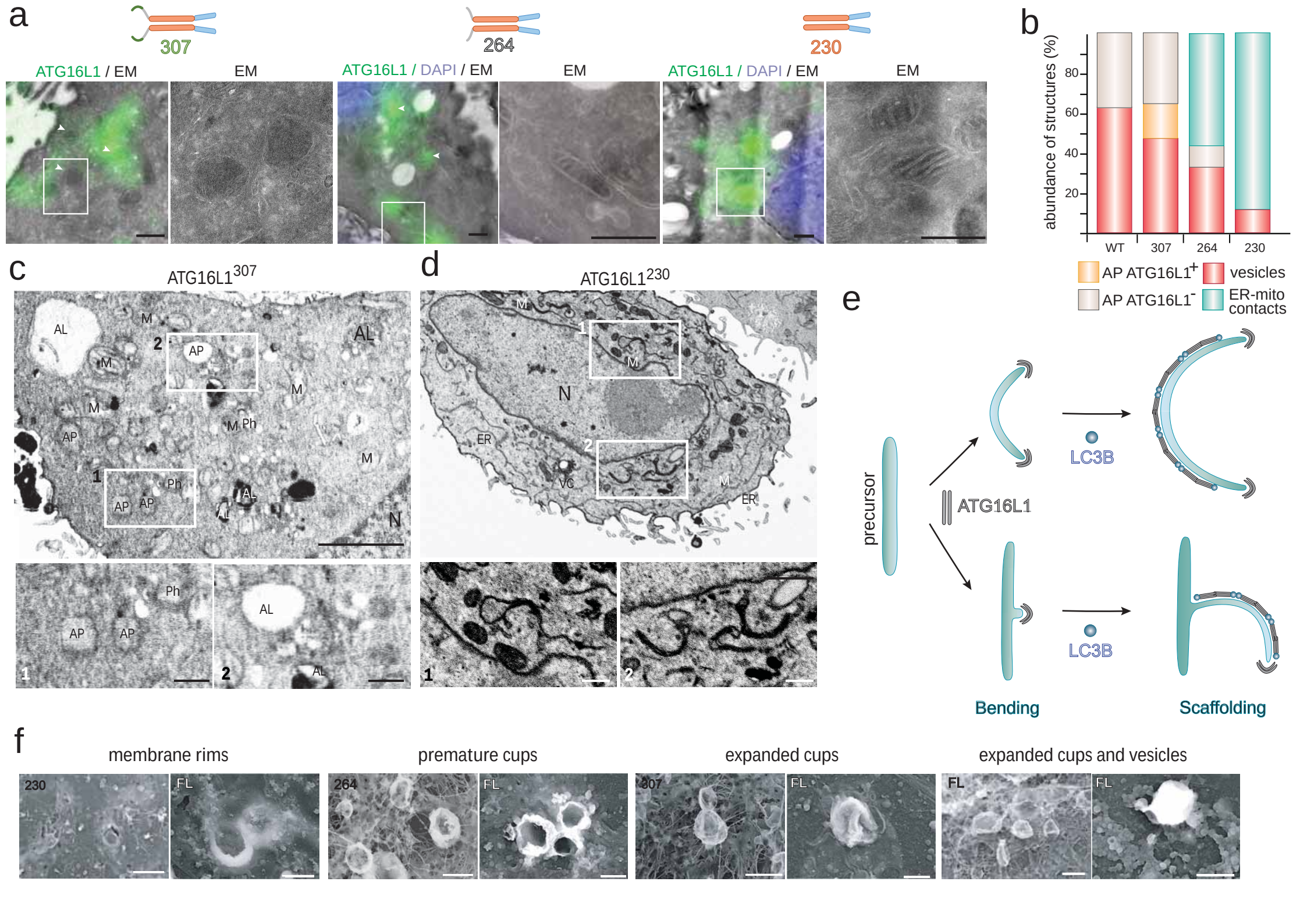
a
307
264
230
ATG16L1 / EM
EM
ATG16L1 / DAPI / EM
EM
ATG16L1 / DAPI / EM
EM
b
abundance of structures (%)
80
60
40
20
WT
307
264
230
AP ATG16L1+
vesicles
AP ATG16L1-
ER-mito contacts
c
ATG16L1307
AL
M
AP
Ph
N
1
2
d
ATG16L1230
M
N
ER
VC
e
precursor
ATG16L1
LC3B
LC3B
Bending
Scaffolding
f
membrane rims
premature cups
expanded cups
expanded cups and vesicles
230
264
307
FL

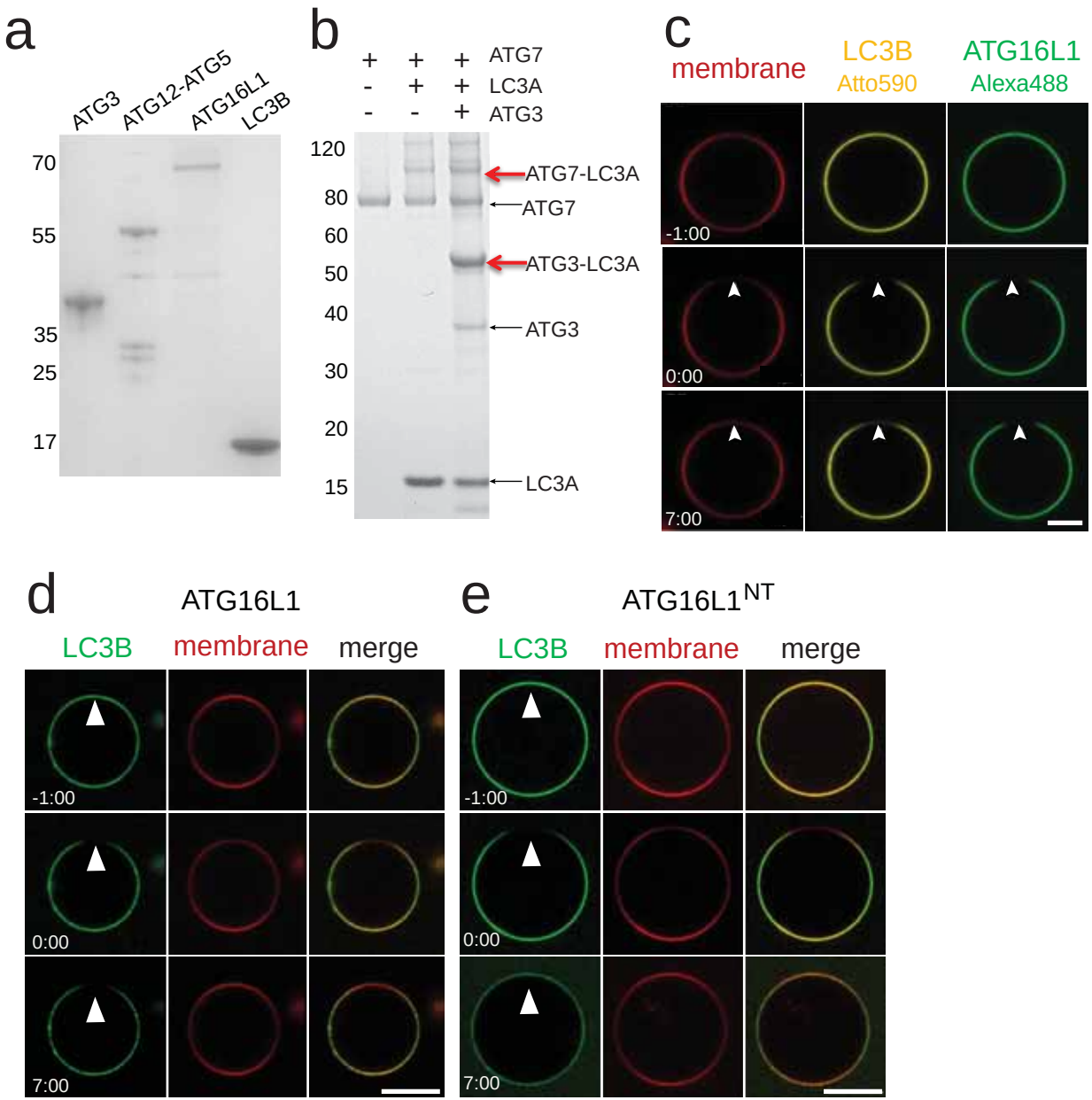
a
ATG3
ATG12-ATG5
ATG16L1
LC3B
70
55
35
25
17
b
+ + + ATG7
- + + LC3A
- - + ATG3
120
80
60
50
40
30
20
15
ATG7-LC3A
ATG7
ATG3-LC3A
ATG3
LC3A
c
membrane
LC3B
Atto590
ATG16L1
Alexa488
-1:00
0:00
7:00
d
ATG16L1
LC3B
membrane
merge
-1:00
0:00
7:00
e
ATG16L1NT
LC3B
membrane
merge
-1:00
0:00
7:00

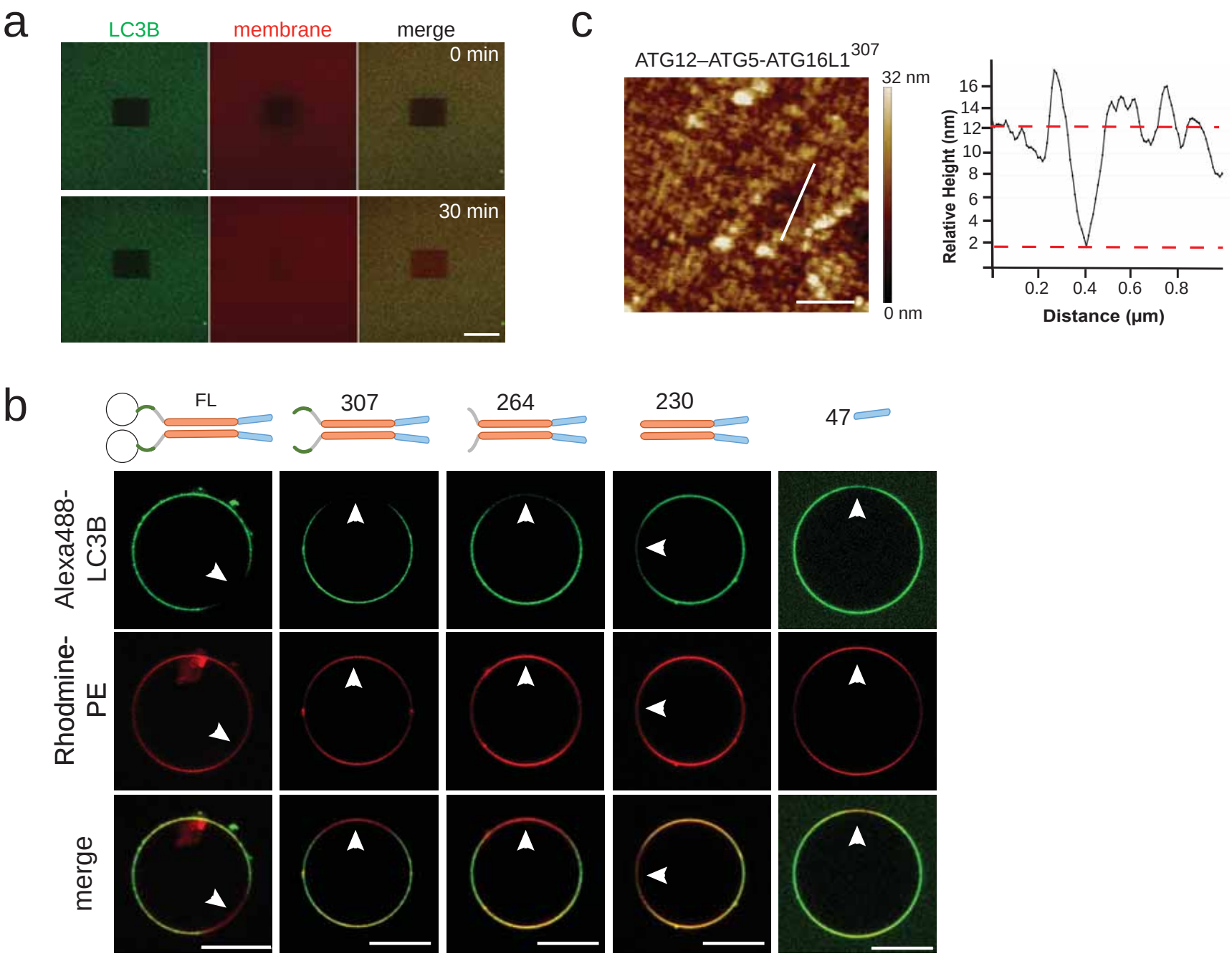
a
LC3B
membrane
merge
0 min
30 min
c
ATG12–ATG5-ATG16L1307
32 nm
0 nm
Relative Height (nm)
16
14
12
10
8
6
4
2
0.2
0.4
0.6
0.8
Distance (μm)
b
FL
307
264
230
47
Alexa488-LC3B
Rhodmine-PE
merge

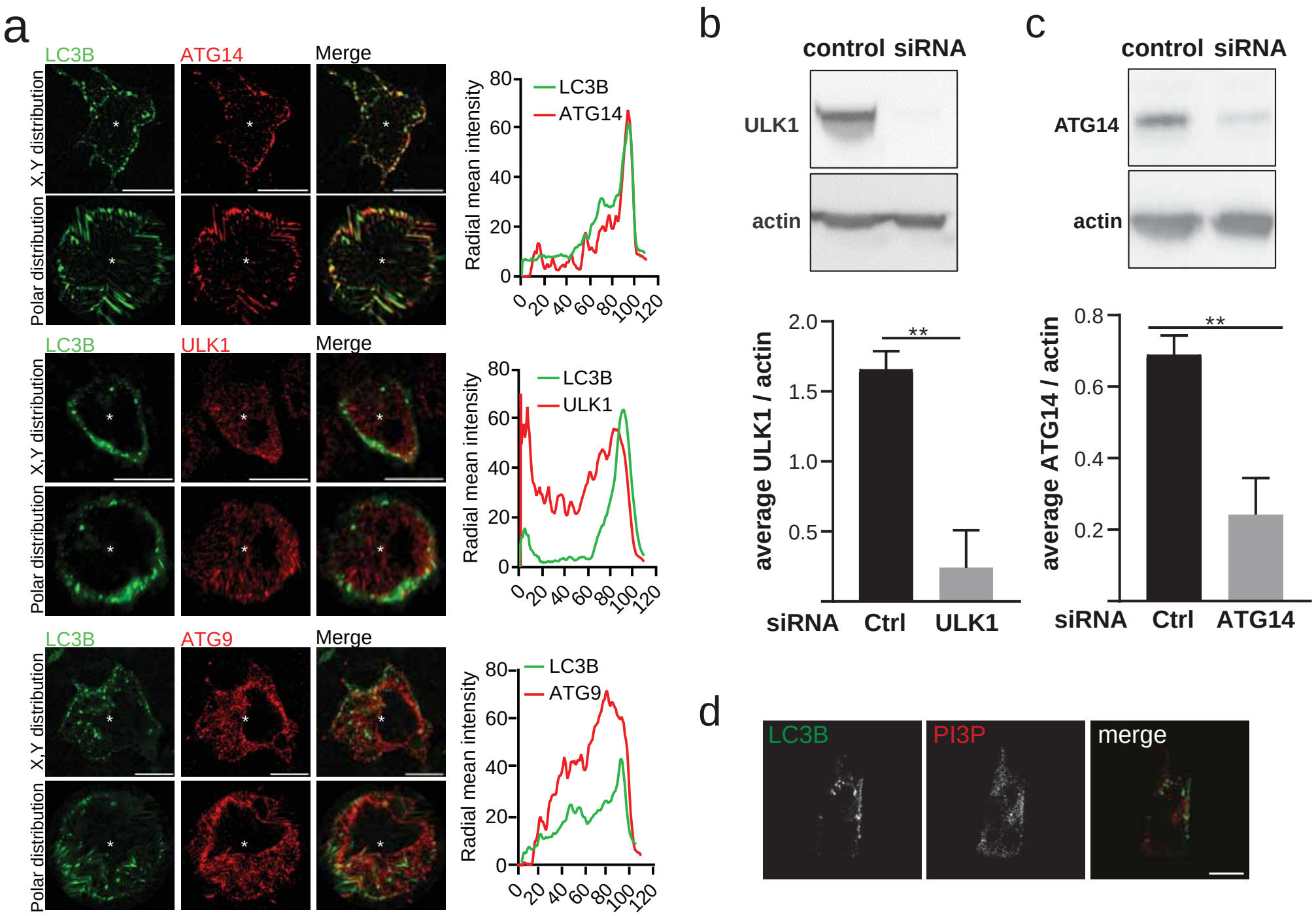
a
LC3B
ATG14
Merge
X,Y distribution
Polar distribution
Radial mean intensity
LC3B
ATG14
ULK1
ATG9
b
control siRNA
ULK1
actin
average ULK1 / actin
siRNA
Ctrl
ULK1
c
control siRNA
ATG14
actin
average ATG14 / actin
siRNA
Ctrl
ATG14
d
LC3B
PI3P
merge

a

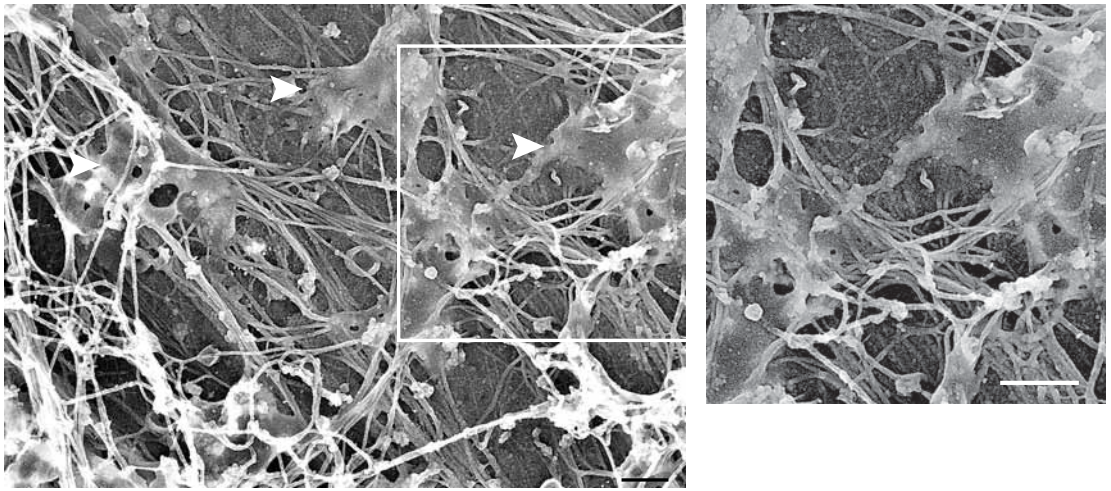

b

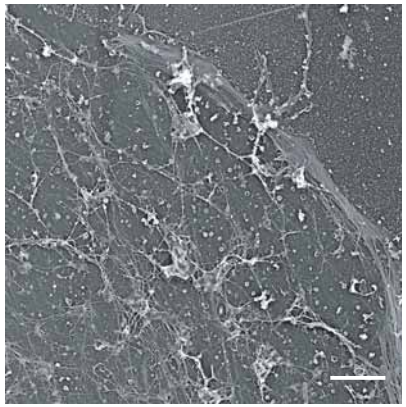

a
ATG16L1
LC3B
PREM
CLEM
b
ATG16L1
LC3B
PREM
CLEM

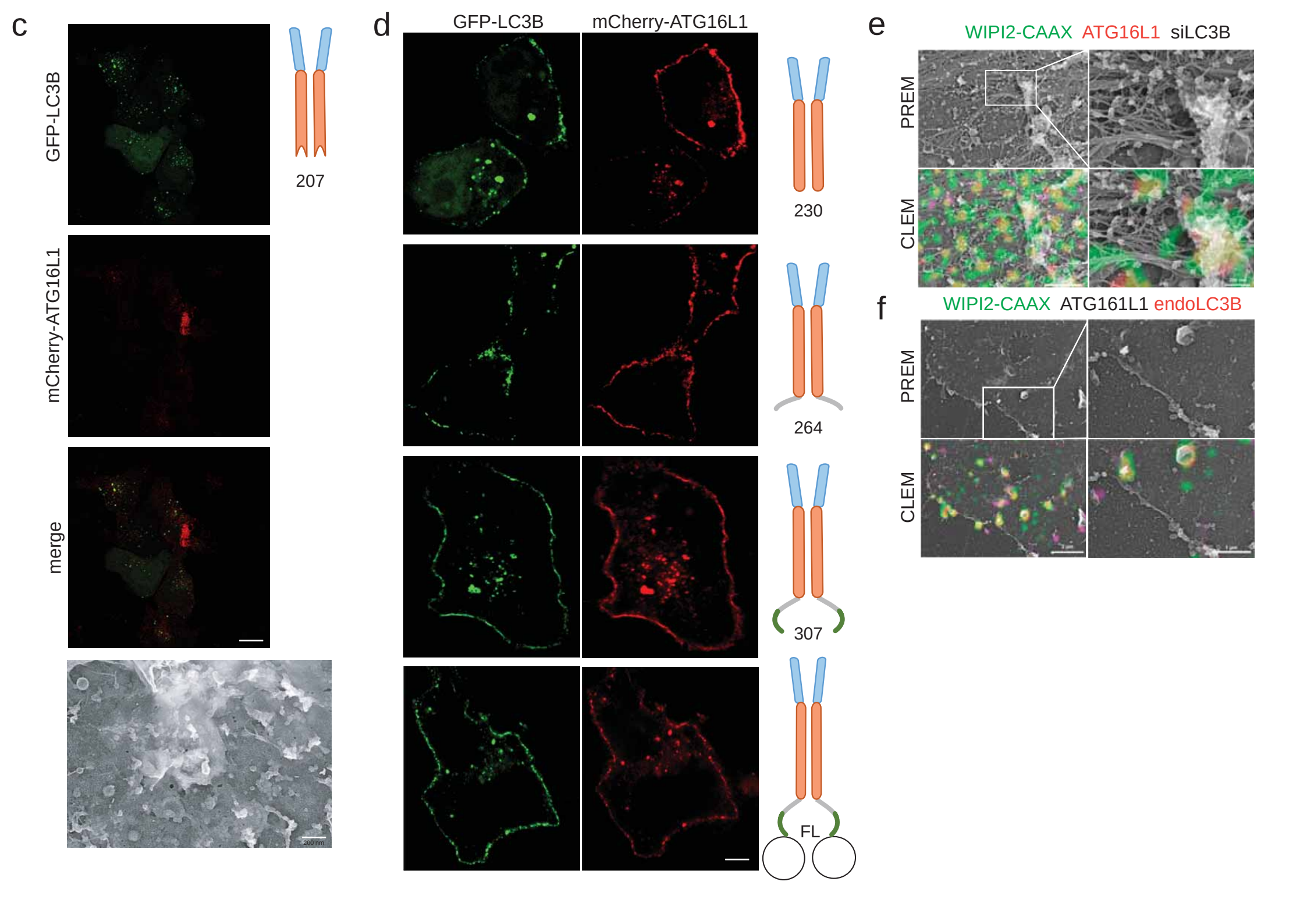
c
GFP-LC3B
mCherry-ATG16L1
merge
207
200 nm
d
GFP-LC3B
mCherry-ATG16L1
230
264
307
FL
e
WIPI2-CAAX ATG16L1 siLC3B
PREM
CLEM
f
WIPI2-CAAX ATG161L1 endoLC3B
PREM
CLEM

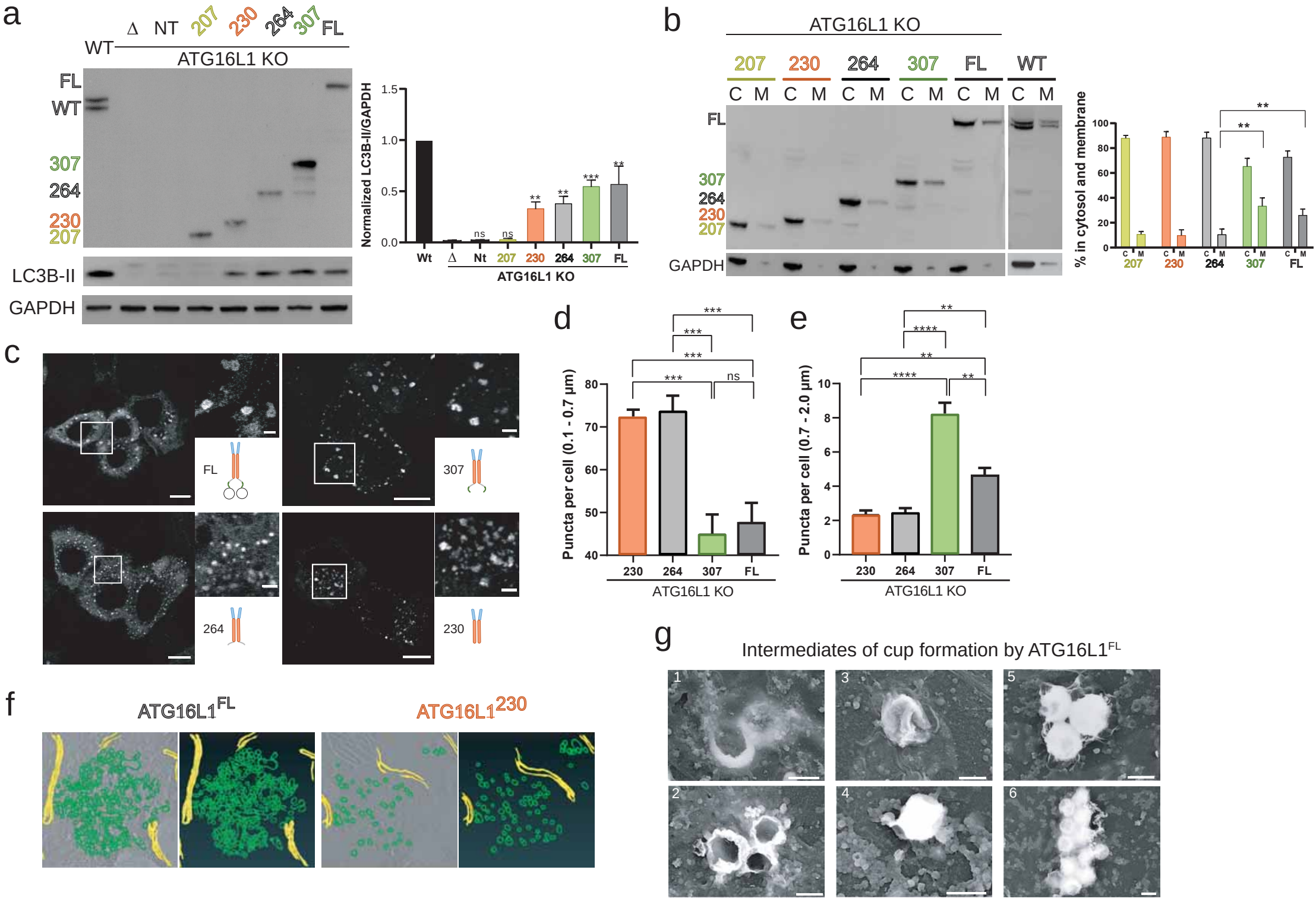
a
Δ NT 207 230 264 307 FL
WT
ATG16L1 KO
FL
WT
307
264
230
207
LC3B-II
GAPDH
Normalized LC3B-II/GAPDH
1.5
1.0
0.5
0.0
ns
ns
**
**
***
**
Wt Δ Nt 207 230 264 307 FL
ATG16L1 KO
b
ATG16L1 KO
207 230 264 307 FL WT
C M C M C M C M C M C M
FL
307
264
230
207
GAPDH
% in cytosol and membrane
100
80
60
40
20
0
**
**
**
C M C M C M C M C M
207 230 264 307 FL
c
FL
307
264
230
d
Puncta per cell (0.1 - 0.7 µm)
80
70
60
50
40
***
***
***
***
ns
230 264 307 FL
ATG16L1 KO
e
Puncta per cell (0.7 - 2.0 µm)
10
8
6
4
2
0
**
****
**
****
**
230 264 307 FL
ATG16L1 KO
f
ATG16L1FL
ATG16L1230
g
Intermediates of cup formation by ATG16L1FL
1
2
3
4
5
6

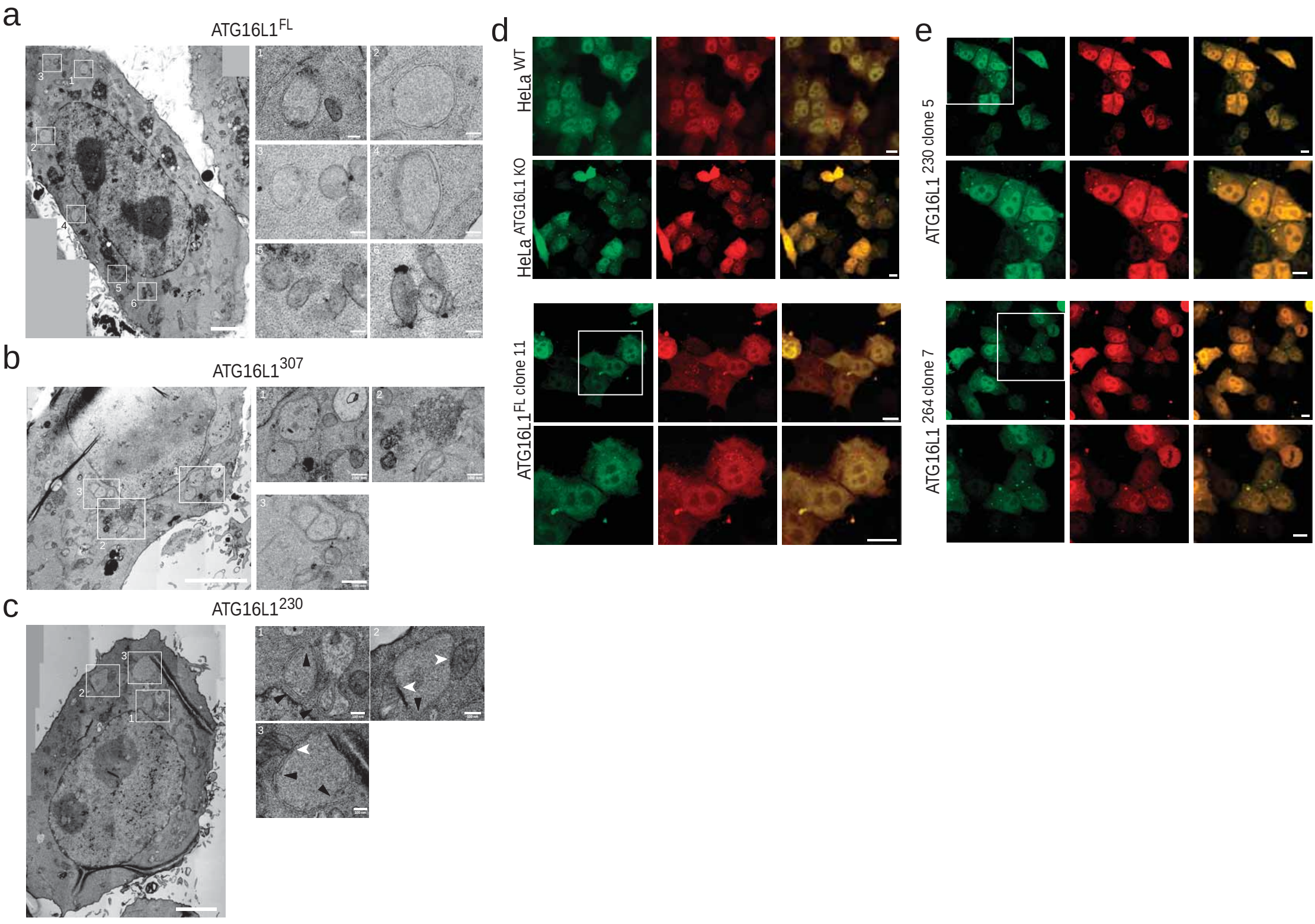
a
ATG16L1FL
b
ATG16L1307
c
ATG16L1230
d
HeLa WT
HeLa ATG16L1 KO
ATG16L1FL clone 11
e
ATG16L1 230 clone 5
ATG16L1 264 clone 7

Extended Data Fig. 3 b, c

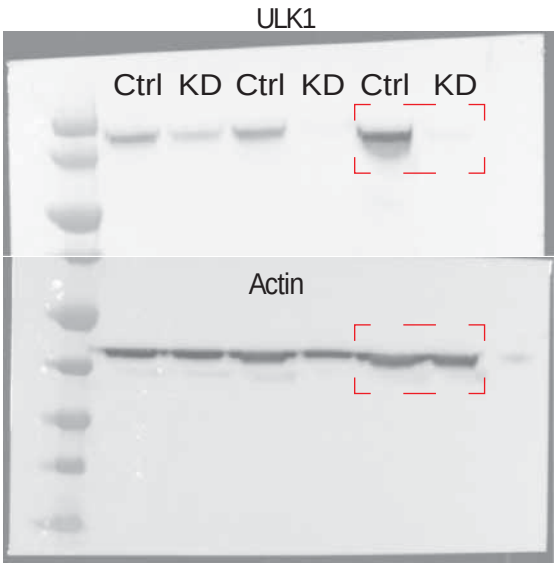

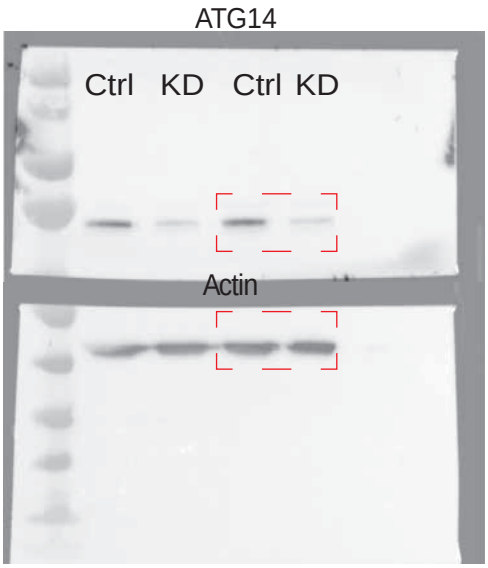

Extended Data Fig. 6a

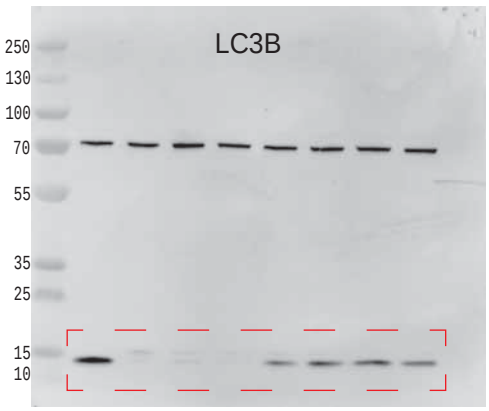

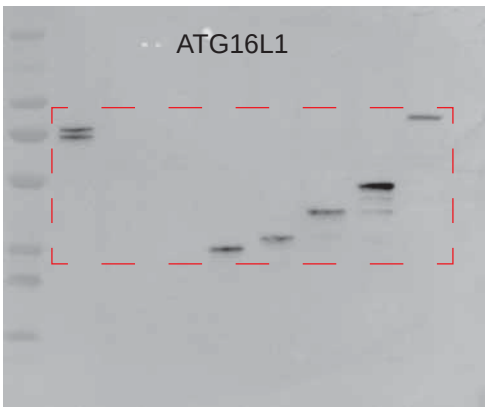

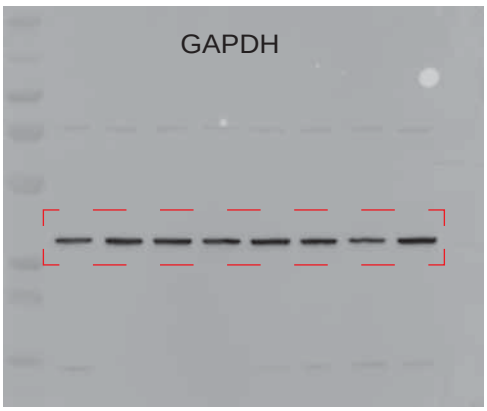

Extended Data Fig. 6b